Atmos. Chem. Phys. Discuss., 11, 3399–3459, 2011
www.atmos-chem-phys-discuss.net/11/3399/2011/
doi:10.5194/acpd-11-3399-2011


Atmospheric Chemistry and Physics Discussions



# Aerosol indirect effects in a multi-scale aerosol-climate model PNNL-MMF

**M. Wang[1], S. Ghan[1], M. Ovchinnikov[1], X. Liu[1], R. Easter[1], E. Kassianov[1], Y. Qian[1], and H. Morrison[2]**

[1]Atmospheric Science and Global Change Division, Pacific Northwest National Laboratory, Richland, Washington, USA
[2]Mesoscale and Microscale Meteorology Division, National Center for Atmospheric Research, Boulder, Colorado, USA

Received: 14 January 2011 – Accepted: 19 January 2011 – Published: 31 January 2011

Correspondence to: M. Wang (minghuai.wang@pnl.gov)

Published by Copernicus Publications on behalf of the European Geosciences Union.







## Abstract

Much of the large uncertainty in estimates of anthropogenic aerosol effects on climate arises from the multi-scale nature of the interactions between aerosols, clouds and large-scale dynamics, which are difficult to represent in conventional global climate models (GCMs). In this study, we use a multi-scale aerosol-climate model that treats aerosols and clouds across multiple scales to study aerosol indirect effects. This multi-scale aerosol-climate model is an extension of a multi-scale modeling framework (MMF) model that embeds a cloud-resolving model (CRM) within each grid cell of a GCM. The extension allows the explicit simulation of aerosol/cloud interactions in both stratiform and convective clouds on the global scale in a computationally feasible way. Simulated model fields, including liquid water path (LWP), ice water path, cloud fraction, shortwave and longwave cloud forcing, precipitation, water vapor, and cloud droplet number concentration are in agreement with observations. The new model performs quantitatively similar to the previous version of the MMF model in terms of simulated cloud fraction and precipitation. The simulated change in shortwave cloud forcing from anthropogenic aerosols is $-0.77\,\mathrm{W\,m^{-2}}$, which is less than half of that in the host GCM (NCAR CAM5) ($-1.79\,\mathrm{W\,m^{-2}}$) and is also at the low end of the estimates of most other conventional global aerosol-climate models. The smaller forcing in the MMF model is attributed to its smaller increase in LWP from preindustrial conditions (PI) to present day (PD): 3.9% in the MMF, compared with 15.6% increase in LWP in large-scale clouds in CAM5. The much smaller increase in LWP in the MMF is caused by a much smaller response in LWP to a given perturbation in cloud condensation nuclei (CCN) concentrations from PI to PD in the MMF (about one-third of that in CAM5), and, to a lesser extent, by a smaller relative increase in CCN concentrations from PI to PD in the MMF (about 26% smaller than that in CAM5). The smaller relative increase in CCN concentrations in the MMF is caused in part by a smaller increase in aerosol lifetime from PI to PD in the MMF, a positive feedback in aerosol indirect effects induced by cloud lifetime effects. The smaller response in LWP to anthropogenic aerosols in





ACPD
11, 3399–3459, 2011



the MMF model is consistent with observations and with high resolution model studies, which may indicate that aerosol indirect effects simulated in conventional global climate models are overestimated and point to the need to use global high resolution models, such as MMF models or global CRMs, to study aerosol indirect effects. The simulated total anthropogenic aerosol effect in the MMF is $-1.05\,\mathrm{W\,m^{-2}}$, which is close to the Murphy et al. (2009) inverse estimate of $-1.1 \pm 0.4\,\mathrm{W\,m^{-2}}$ ($1\sigma$) based on the examination of the Earth's energy balance. Further improvements in the representation of ice nucleation and low clouds are needed.

## 1 Introduction

Clouds are an extremely important climate regulator. They have a large impact on the Earth's energy budget and play a central role in the hydrological cycle. By acting as cloud condensation nuclei (CCN) or ice nuclei, anthropogenic aerosols can modify cloud optical and physical properties, and therefore affect the climate system, giving rise to the so-called the aerosol indirect effect. Uncertainties in estimates of the anthropogenic aerosol indirect effect still dominate uncertainties in the estimates of radiative forcing of past and future climate change, despite more than a decade of effort on this issue (Forster et al., 2007; IPCC, 2007; Lohmann et al., 2010).

Much of this uncertainty arises from the multi-scale nature of the interactions between aerosol, clouds, and large-scale dynamics. These interactions span a wide range in spatial scales, from 0.01–10 µm for droplet and crystal nucleation, to 10–1000 m for turbulence-driven updrafts, to 2–10 km for deep convection, to 50–100 km for large-scale cloud systems. Given the typical global climate model (GCM) grid spacing of a hundred kilometers, the treatment of most of those processes is highly parameterized in conventional GCMs and therefore may not be accurate.

One example is cloud lifetime effects of aerosol. As implemented in most GCMs, cloud lifetime effects assume that, because of less efficient coalescence and collection among cloud droplets, increasing cloud droplet number concentrations from





ACPD
11, 3399–3459, 2011



anthropogenic aerosols always slows formation of precipitation and increases liquid water path (LWP) and cloud lifetime (Albrecht, 1989). However, observations show evidence of both decreasing and increasing LWP with increasing aerosols (Platnick et al., 2000; Coakley and Walsh, 2002; Kaufman et al., 2005; Matsui et al., 2006), and cloud resolving model (CRM) studies show that whether LWP increases or decreases with increasing aerosols depends on meteorological conditions (Ackerman et al., 2004; Xue et al., 2008; Small et al., 2009).

It is even more problematic to represent aerosol/cloud processes in deep cumulus clouds in GCMs. Cumulus parameterizations in current climate models rely on ad hoc closure assumptions designed to diagnose the latent heating and vertical transport of heat and moisture by deep convection, and provide little information about microphysics or updraft velocity (Emanuel and Zivkovic-Rothman, 1999; Del Genio et al., 2005; Zhang et al., 2005). As a result, only a handful of GCMs have treated aerosol effects on convective clouds in their estimates of aerosol indirect effects (Menon and Rotstayn, 2006; Lohmann, 2008), and because those treatments were based on conventional cumulus parameterizations, the treatments are quite crude. Menon and Rotstayn (2006) introduced a physically-based treatment of aerosol effects on convective cloud microphysics in two GCMs and found a strong dependence of indirect effects on the details of the cumulus parameterization: including aerosol effects on convective clouds increased aerosol indirect effects in one GCM but slightly decreased aerosol indirect effects in the other GCM. Lohmann (2008) investigated aerosol effects on convective clouds by extending a double-moment cloud microphysics scheme developed for stratiform clouds to convective clouds, and found that including aerosol effects in convective clouds reduces the sensitivity of the LWP to aerosol optical depth (AOD), which is in better agreement with observations and large-eddy simulation studies and leads to slightly smaller total aerosol forcing. Clearly, more physically based modeling studies are needed to better quantify the response of all cloud types to changes in aerosol loading and to narrow down the aerosol indirect effect estimates.





ACPD
11, 3399–3459, 2011



We have recently developed a multi-scale aerosol-climate model (Wang et al., 2010), which is an extension of a multi-scale modeling framework (MMF) model that embeds a CRM within each grid column of a GCM (Khairoutdinov et al., 2008). The GCM component includes a modal aerosol treatment that uses several log-normal modes to represent aerosol size distributions. The CRM component has a two-moment microphysics scheme and predicts both mass and number mixing ratios for all hydrometeor types. Cloud statistics diagnosed from the CRM component are used to drive the aerosol and trace gas processing by clouds. This multi-scale aerosol-climate model allows us to explicitly simulate aerosol/cloud interactions in both stratiform and convective clouds. Compared to global CRMs with on-line aerosols (Suzuki et al., 2008), this multi-scale aerosol-climate model is computationally much more feasible for running multi-year climate simulations. Wang et al. (2010) showed that this multi-scale aerosol-climate model simulates aerosol fields as well as conventional aerosol-climate models.

In this study, we evaluate simulated cloud fields from this multi-scale aerosol-climate model, and examine anthropogenic aerosol effects on clouds and climate. Section 2 describes the model. Model results with the present day aerosol and precursor emissions are shown in Sect. 3. The aerosol indirect effects are examined in Sect. 4 and finally the results are summarized in Sect. 5.

## 2 Model description and set-up of simulations

### 2.1 Model description

The PNNL-MMF is documented in detail in Wang et al. (2010) and is only briefly described here. It is an extension of the Colorado State University (CSU) MMF model (Randall et al., 2003; Khairoutdinov et al., 2005, 2008; Tao et al., 2009), first developed by Khairoutdinov and Randall (2001). The host GCM in the PNNL-MMF is the Community Atmospheric Model version 5 (CAM5) (http://www.cesm.ucar.edu/models/cesm1.0/cam/), which is the atmospheric component of the Community Earth System Model





ACPD
11, 3399–3459, 2011



(CESM1.0). The embedded CRM in each GCM grid column is a two-dimensional version of the System for Atmospheric Modeling (SAM) (Khairoutdinov and Randall, 2003), which replaces the conventional moist physics, convective cloud, turbulence, and boundary layer parameterizations in CAM5. During each GCM time step (every 10 min), the CRM is forced by the large-scale temperature and moisture tendencies arising from GCM-scale dynamical processes and feeds the cloud response back to the GCM-scale as heating and moistening terms in the large-scale budget equations for heat and moisture. The CRM runs continuously using a 20-s time step.

The version of the SAM CRM used in this study features a two-moment cloud microphysics scheme (Morrison et al., 2005, 2009), which replaces the simple bulk microphysics used in the original CSU MMF model. The new scheme predicts the number concentrations and mass mixing ratios of five hydrometeor types (cloud droplets, ice crystals, rain droplets, snow particles, and graupel particles). The precipitation hydrometeor types (rain, snow, and graupel) are fully prognostic in the CRM model, rather than diagnostic in CAM5 (Morrison and Gettelman, 2008). Droplet activation from hydrophilic aerosols, ice nucleation, ice crystal growth by vapor deposition, the dependence of ice crystal sedimentation on crystal number, and the dependence of autoconversion on droplet number are treated. Several ice nucleation mechanisms are included: contact nucleation of cloud droplets following Morrison and Pinto (2005); immersion freezing of cloud droplets and rain following Bigg (1953); deposition-condensation freezing nucleation following Thompson et al. (2004), which is based on ice crystal concentration measurements of Cooper (1986) and limited to a maximum of $0.5\,\mathrm{cm}^{-3}$; and homogenous freezing of all cloud and rain drops below $-40\,^{\circ}\mathrm{C}$. These ice nucleation treatments do not directly link heterogeneous ice nuclei to aerosols. Droplet activation is calculated at each CRM grid cell, based on the parameterization of Abdul-Razzak and Ghan (2000). The vertical velocity for calculating droplet activation is related to the resolved vertical velocity and the turbulence kinetic energy, with a minimum vertical velocity of $0.1\,\mathrm{m\,s}^{-1}$. Aerosol fields used in droplet activation in the CRM are predicted on the GCM grid cells as described next.





ACPD
11, 3399–3459, 2011



CAM5, the driving GCM, uses a modal approach to treat aerosols (Liu et al., 2011) on the CAM5 grid. Aerosol size distributions are represented by using three log-normal modes: an Aitken mode, an accumulation mode, and a single coarse mode. Aitken mode species include sulfate, secondary organic aerosol (SOA), and sea salt; accumulation mode species include sulfate, SOA, black carbon (BC), primary organic matter (POM), sea salt, and dust; coarse mode species include sea salt, dust, and sulfate. Species mass and number mixing ratios are predicted for each mode, while mode widths are prescribed. Aerosols outside cloud droplets (interstitial) and aerosols within cloud droplets (cloud-borne) are both predicted. Aerosol nucleation (involving $H_2SO_4$ vapor), condensation of trace gases ($H_2SO_4$ and semi-volatile organics) on existing aerosol particles, and coagulation (Aitken and accumulation modes) are also treated.

In the PNNL MMF, the treatment of cloud-related aerosol and trace gas processes (i.e., aqueous chemistry, convective transport, and wet scavenging) in the standard CAM5 is replaced by the explicit-cloud-parameterized-pollutant (ECPP) approach (Gustafson et al., 2008; Wang et al., 2010). The ECPP approach uses statistics of cloud distribution, vertical velocity, and cloud microphysical properties resolved by the CRM to drive aerosol and chemical processing by clouds on the GCM grid, which allows us to explicitly treat the effects of convective clouds on aerosols in computationally feasible manner. The ECPP approach predicts both interstitial aerosols and cloud-borne aerosols in all clouds, while the conventional CAM5 only treats cloud-borne aerosols in stratiform clouds. In addition, by integrating the continuity equation for aerosols and trace gases in convective updraft and downdraft regions, the ECPP approach treats convective transport, aqueous chemistry, and wet scavenging in an integrated, self-consistent way (Wang et al., 2010).

The CAM5 radiative transfer scheme uses the Rapid Radiative Transfer Model for GCMs (RRTMG), a broadband *k*-distribution radiation model developed for application to GCMs (Mlawer et al., 1997; Iacono et al., 2003, 2008). The CAM5 radiative transfer calculation is applied to each CRM column at each GCM time step (10 min), assuming 1 or 0 cloud fraction at each CRM grid cell. Aerosol optical properties are diagnosed





ACPD
11, 3399–3459, 2011



on the CRM grid from the dry aerosol on the GCM grid, and the aerosol water on the CRM grid that is calculated from Kohler theory based on the relative humidity on the CRM grid, accounting for hysteresis and the hygroscopicities of each of the modes' components (Ghan and Zaveri, 2007).

## 2.2 Emissions and set-up of simulations

The host GCM CAM5 uses a finite-volume dynamical core, with 30 vertical levels at $1.9^{\circ} \times 2.5^{\circ}$ horizontal resolution. The GCM time step is 10 min. Climatological sea surface temperature and sea ice are prescribed. The embedded CRM includes 32 columns at 4-km horizontal grid spacing and 28 vertical layers coinciding with the lowest 28 CAM levels. The time step for the embedded CRM is 20 s. The MMF model was integrated for 36 months. Results from the last 34 months are used in this study. Results from the MMF model are also compared with those from the conventional CAM5. The conventional CAM5 runs at $1.9^{\circ} \times 2.5^{\circ}$ horizontal resolution with 30 vertical levels and a time step of 30 min, and was integrated for 5 years. Results from the last four years are reported here. The three-mode aerosol scheme and the modified Morrison-Gettelman two-moment cloud scheme are used for large-scale processes in CAM5 (Gettelman et al., 2010), and shallow and deep convective clouds are parameterized with no explicit aerosol effects.

Both the MMF and CAM5 use the same aerosol and precursor emissions as described in Liu et al. (2011) and Wang et al. (2010). Anthropogenic $SO_2$, BC, and primary organic carbon emissions are from the Lamarque et al. (2010) IPCC AR5 emission data set. The years 2000 and 1850 are chosen to represent the present day (PD) and the pre-industrial (PI) time, respectively. Volcanic $SO_2$ and DMS emissions are taken from Dentener et al. (2006), and 2.5% of $SO_2$ emissions are emitted as primary sulfate aerosol. Aerosol number emissions are derived from mass emissions using species densities and volume mean emission diameters, which vary with species and emission sector. In the simplified SOA mechanism in CAM5 (Liu et al., 2011), gas-phase SOA (g) is emitted directly in the model using prescribed yields for several





ACPD
11, 3399–3459, 2011



primary volatile organic compound (VOC) classes (Liu et al., 2011), rather than being formed by atmospheric oxidation. The VOC emissions are taken from the MOZART-2 data set (Horowitz et al., 2003). Gas-phase SOA (g) partitions to the aerosol phase to form SOA aerosol through the thermodynamical transfer process. Emissions of sea salt and mineral dust aerosols are calculated online. The sea salt emissions parameterization follows Martensson et al. (2003) and particles with diameters between 0.02–0.08, 0.08–1.0, and 1.0–10.0 µm are placed in the Aitken, accumulation, and coarse modes, respectively. Mineral dust emissions are calculated with the Dust Entrainment and Deposition Model (Zender et al., 2003); the implementation in CAM has been described in Mahowald et al. (2006a, b) and Yoshioka et al. (2007). Dust particles with diameters between 0.1–1.0 and 1.0–10.0 µm are placed in the accumulation and coarse modes, respectively.

Two simulations are performed for both the MMF and CAM5: one with the PD aerosol and precursor emissions, and the other with the PI aerosol and precursor emissions. Greenhouse gases are fixed at the present day level in all simulations.

## 3 Model results in the PD simulations

### 3.1 Cloud fields

#### 3.1.1 Global and annual averages

Table 1 lists global annual means of simulated cloud and radiation parameters in the MMF, along with those from the conventional CAM5 and observations. The liquid water path (LWP) in the MMF simulation is 55.9 g m$^{-2}$, which is slightly larger than the total LWP (large-scale + convective clouds) simulated by CAM5 (48.4 g m$^{-2}$) and is in the observed range of 50–84 g m$^{-2}$. Cloud-top droplet number concentration for low level (cloud-top pressure higher than 640 hPa), and warm (cloud-top temperature warmer than 273.16 K) clouds in the MMF is 109 cm$^{-3}$, which is slightly lower than that





ACPD
11, 3399–3459, 2011



in CAM5 (121 $cm^{-3}$). Cloud-top droplet effective radius in the MMF is 9.2 µm, which is slightly smaller than that in CAM5 (9.7 µm), and both underestimate observations (11.4–15.7 µm). Simulated column-integrated grid-mean cloud droplet number concentration ($2.3 \times 10^{10}$ $m^{-2}$) is nearly 50% higher than that in CAM5 ($1.6 \times 10^{10}$ $m^{-2}$). The large difference in column-integrated cloud droplet number concentrations between the MMF and CAM5 can be partly explained by the fact that column-integrated cloud droplet number concentration in CAM5 only includes contributions from large-scale clouds while the MMF includes contributions from both large-scale and convective clouds.

Simulated cloud ice water path, snow water path, and graupel water path are 9.9, 53.4, and 5.7 $g\,m^{-2}$, respectively. The total frozen water path is 69.0 $g\,m^{-2}$ and is close to that simulated in CAM5 (61.3 $g\,m^{-2}$). It is also close to that retrieved from CloudSat (around 80 $g\,m^{-2}$), and MODIS (60 $g\,m^{-2}$), but is much larger than estimates from ISCCP (around 35 $g\,m^{-2}$) and NOAA NESDIS (around 10 $g\,m^{-2}$) (Fig. 18 in Waliser et al., 2009). CloudSat retrievals are sensitive to large hydrometeor particles and are considered to be more representative of total frozen water (Waliser et al., 2009). The partitioning of total frozen water among different ice hydrometeor components is similar to that in the NASA fvMMF model (Waliser et al., 2009), which is another MMF model treating multiple hydrometeor types (Tao et al., 2009). Both the PNNL MMF and NASA fvMMF simulate a small contribution from cloud ice water over the tropics (30° S–30° N) (13% in the PNNL MMF, compared with 10% in the NASA fvMMF). However, the PNNL MMF produces a much smaller contribution from graupel (14%), compared with that in the NASA fvMMF (50%). These differences may result from the differences in the microphysics schemes in the CRM components in the two MMF models. Given the fact that no global observation is able to distinguish different ice hydrometeors, it is still difficult to constrain the partitioning among different hydrometeors in GCMs.

Simulated column-integrated ice crystal number concentration is $0.021 \times 10^{10}$ $m^{-2}$, which is twice that in CAM5. The ice nucleation treatment in the MMF model does not directly link heterogeneous ice nuclei to aerosols although aerosols can influence





ACPD
11, 3399–3459, 2011



ice crystal number concentration through the freezing of cloud droplets activated on aerosols. In CAM5, sulfate can form ice crystals in cirrus clouds through homogeneous freezing, and dust can act as heterogeneous ice nuclei in cirrus and mixed-phase clouds (Gettelman et al., 2010). Large uncertainties exist in simulated column-integrated ice crystal number concentrations in global climate models (ranges 0.1–$0.7 \times 10^{10}\,m^{-2}$ in Lohmann et al. (2008); 0.02–$0.09 \times 10^{10}\,m^{-2}$ in Wang and Penner, 2010). Heterogeneous nucleation in cirrus clouds generally leads to lower column-integrated ice crystal number concentrations in better agreement with observed ice crystal number concentrations in the upper troposphere (Wang and Penner, 2010). Aerosol effects on ice nucleation in the MMF will be the subject of a future study.

The total cloud fraction is 55.8%, which is smaller than that in CAM5 (62.7%) and in observations (65–75%). Simulated high cloud fraction, 29.2%, is smaller than that in CAM5. Shortwave cloud forcing is $-50.5\,W\,m^{-2}$, which is in the observed range ($-47$ to $-54\,W\,m^{-2}$) and is close to that in CAM5 ($-50\,W\,m^{-2}$). Simulated longwave cloud forcing is $26\,W\,m^{-2}$, slightly smaller than ERBE ($30\,W\,m^{-2}$) and CERES ($29\,W\,m^{-2}$) observations, and is larger than that simulated in CAM5 ($22\,W\,m^{-2}$). Simulated precipitation rate is 2.85 mm day$^{-1}$, higher than observations (2.61 mm day$^{-1}$).

### 3.1.2 Global and zonal distributions

Figures 1 and 2 show annual average zonal mean latitude-pressure cross sections for grid-averaged hydrometeor mass and number concentrations, respectively. Simulated cloud liquid water mass concentrations peak over the tropics and mid-latitude storm tracks at 800–900 hPa, which is similar to that of liquid droplet number concentrations, though the latter demonstrates the stronger influence of anthropogenic aerosols as cloud droplet number concentrations are higher in the Northern Hemisphere (NH) than in the Southern Hemisphere (SH). Rain water is more concentrated over the tropics, though rain droplet number concentrations peak over the SH mid-latitudes and over the NH high latitudes, which indicates that rain droplet size is larger over the tropics than over the middle and high latitudes. Rain formation over the high latitudes is likely





ACPD
11, 3399–3459, 2011



dominated by warm collision-coalescence processes and drizzle from low clouds rather than melting from graupel and snow, which leads to low rain mass mixing ratios and high rain droplet number concentrations.

Simulated cloud ice mass concentrations peak in the upper troposphere over the tropics, while ice crystal number concentrations peak over both the tropics and high latitudes because of colder temperatures over these regions. Snow water mass dominates the total ice water in the MMF model, as we discussed in Sect. 3.1, and graupel has a small contribution to the total ice water. The total ice water distribution shows a peak at 400–500 hPa over the tropics, and two other peaks over the mid-latitude storm track regions, which are in reasonable agreement with the total ice water distribution from CloudSat (Waliser et al., 2009; Gettelman et al., 2010). The spatial distributions of the different ice hydrometeors are qualitatively similar to those from the NASA fvMMF (Fig. 12 in Waliser et al., 2009), except that the NASA fvMMF simulates a large contribution from graupel.

Figure 3 compares simulated annual mean total cloud cover with the ISCCP observations. The total cloud cover in the MMF is diagnosed based on column-integrated total cloud water path (liquid + ice) at each CRM column. Columns are considered cloudy if the total cloud water path is larger than 1 g m$^{-2}$ and clear otherwise. The instantaneous total cloud cover is defined as a ratio of cloudy columns to the total number of columns in the CRM (32 in the current setup). The simulated spatial pattern of total cloud cover is in reasonable agreement with observations, but in general, the model underestimates cloud fraction. The underestimation is especially true over regions where low clouds dominate, such as over the subtropical regions in which trade cumulus and stratocumulus are observed. This underestimation was also evident in several previous MMF studies (Khairoutdinov et al., 2005, 2008). This is caused in part by the the coarse CRM horizontal resolution (4 km), which makes it difficult to simulate boundary layer clouds in the MMF model.





ACPD
11, 3399–3459, 2011



Figure 4 compares simulated annual mean shortwave and longwave cloud forcings with those from the CERES observations. Shortwave (longwave) cloud forcing is defined as the difference between the shortwave (longwave) clear-sky and all-sky radiative fluxes at the top of the atmosphere. Annual global mean shortwave cloud forcing in the MMF model is larger than the CERES observation ($-0.5$ vs. $-47.1\,W\,m^{-2}$). The MMF model underestimates shortwave cloud forcing over regions with a large amount of low clouds, such as over the subtropical regions, consistent with the underestimation of cloud cover (Fig. 3), while it overestimates shortwave cloud forcing over the tropics. The longwave cloud forcing in the MMF model is smaller than the CERES observation (26.0 vs. $29.9\,W\,m^{-2}$). The radiative effect of snow particles is accounted for in this study, and is included in the cloud forcing. A sensitivity test with the MMF model at a coarse GCM resolution ($4^\circ \times 5^\circ$) shows that including the radiative effect of snow increases the shortwave cloud forcing by about $8\,W\,m^{-2}$ (in the absolute amount) and the longwave cloud forcing by $5\,W\,m^{-2}$ in January.

Figure 5 compares simulated annual-mean precipitation rate and precipitable water with observations. The model reproduces the overall features of the observation. However, the model simulates excessive precipitation over the West Indian Ocean, the Maritime continent, Australia, West Pacific, and East Pacific in the tropics, and West China. The model underestimates precipitation rate over ocean and over land in the subtropics and mid-latitudes. The simulated precipitable water has a similar pattern as that in the observations. However, the model overestimates precipitable water over most of the oceans and the Maritime Continent, and underestimates precipitable water over land in the subtropics. The simulation of precipitation and precipitable water by this version of the MMF model is quantitatively similar to the previous version of MMF (Khairoutdinov et al., 2008). The two-moment cloud microphysics coupled with a modal aerosol treatment in this version of the model does little to improve the simulations of precipitation and precipitable water.

Figure 6 compares simulated annual-mean cloud-top droplet number concentration with that from the MODIS satellite retrievals. The satellite data is derived from version





ACPD
11, 3399–3459, 2011



4 of the MODIS by Quaas et al. (2006). For both the satellite and model data, only warm (>273 K) and low level clouds (pressure > 640 hPa) are sampled. For consistency, the model output is only sampled at the satellite overpass time (13:30 LST). The MMF model reproduces the spatial patterns of the observed cloud-top droplet number concentrations, with larger droplet number concentrations over land than over ocean and over the NH than over the SH, which clearly demonstrates the influence of anthropogenic aerosols. The patterns in gradients are replicated by both the MMF model as well as observations from the anthropogenic sources over land to its downwind sides over marine environments, e.g., Pacific, Atlantic, and Indian Ocean. The MMF model also simulates enhanced droplet number concentrations over the Southern Ocean (around 50° S), consistent with MODIS observations. However, the MMF model overestimates droplet number concentrations over many oceanic regions, such as the Indian Ocean, the tropical Atlantic Ocean and the tropical Pacific Ocean. In contrast, over the oceanic regions, CAM5 simulates fewer cloud droplets than the MMF, and agrees better with the MODIS observations. On the other hand, over the continental regions, CAM5 simulates more cloud droplets than the MMF and overestimates cloud droplet number concentrations compared with the MODIS observations. The differences in simulated cloud-top droplet number concentrations between CAM5 and the MMF are consistent with the differences in simulated CCN concentrations discussed in Sect. 3.2.

### 3.2 Aerosol fields

Simulated aerosol fields in the present day simulation at a coarse GCM horizontal resolution (4° × 5°) were documented and evaluated against observations in Wang et al. (2010), and here we briefly compare the MMF results with CAM5.

The annual, global mean aerosol sources, burdens, and lifetimes are summarized in Table 2. Simulated sulfate, BC, POM and SOA burden in the MMF (CAM5) are 1.05 (0.53) Tg S, 0.14 (0.11) Tg, 1.04 (0.77) Tg, and 1.83 (1.40) Tg, respectively. The lower BC, POM and SOA burdens in CAM5 are due to their larger wet removal rates (not





ACPD
11, 3399–3459, 2011



shown). The lower sulfate burden in CAM5 is partly from a larger wet removal rate, as evident from its shorter lifetime, and partly from smaller sulfate production (42.5 Tg S/yr in CAM5 vs. 59.8 Tg S/yr in the MMF). The latter is caused in part by the difference in the treatment of soluble fraction of $SO_2$. The soluble fraction of $SO_2$ for wet removal is similar to that of $H_2O_2$ in CAM5, which is quite efficient and leads to strong wet removal of $SO_2$, while the soluble fraction of $SO_2$ in the MMF is based on the effective Henry law equilibrium and is much smaller than that of $H_2O_2$, resulting in less wet removal of $SO_2$. It is not surprising that sea salt and dust burden are similar in the MMF and CAM5 since dust and sea salt emissions in the MMF are tuned so their burdens match the CAM5 burdens.

Figure 7 shows aerosol size distributions in the marine boundary layer. The observational data are from Heintzenberg et al. (2000) and were compiled and aggregated onto a $15^{\circ} \times 15^{\circ}$ grid. The model output is sampled over the same regions as those of observations. Aerosol size distributions simulated by both the MMF and CAM5 are in reasonable agreement with observations, and show bimodal distributions in most regions. However, both the MMF and CAM5 underestimate the accumulation mode aerosol number concentrations, especially over the low and mid-latitude bands. This may suggest that the models underestimate fine-mode sea salt, polluted outflow from continents or the growth of Aitken mode particles. Wang et al. (2009) showed that the underestimation of fine-mode sea salt particles in their model was consistent with their underestimation of accumulation mode aerosol number concentrations. Simulated aerosol number concentrations in the MMF are higher than that in CAM5 and agree better with observations. Higher aerosol number concentrations in the MMF are consistent with its higher global aerosol burdens (Table 2).

Figure 8 shows monthly BC concentrations at four sites in the polar regions. BC concentrations in the MMF are in reasonable agreement with observations, in terms of both magnitudes and seasonal cycles. In contrast, CAM5 underestimates BC concentrations by 1–2 orders of magnitude in the polar regions. What is more, CAM5 does not capture the observed seasonal cycle. Simulated sulfate aerosols over the Arctic in





ACPD
11, 3399–3459, 2011



the MMF demonstrate a similar improvement over CAM5 (not shown).

Figure 9 show the annual mean global distribution of CCN concentrations (at 0.1% supersaturation) averaged over the lowest 8 model levels (surface to about 800 hPa) in both the MMF and CAM5. The spatial patterns of CCN concentrations are similar in the MMF and CAM5, with high concentrations over strongly polluted regions, and low concentrations over remote regions. However, the MMF produces lower CCN concentrations in the strongly polluted regions and higher CCN concentrations in the remote regions, such as remote oceanic regions and polar latitudes, than CAM5. The higher CCN concentrations in the polar latitudes in the MMF can also be seen in the annual zonal distribution shown in Fig. 10, which is consistent with higher aerosol concentrations in the polar latitudes discussed above (Fig. 8). It is also evident in Fig. 10 that the MMF produces higher CCN concentrations at high altitudes than CAM5.

## 4 Aerosol indirect effects

### 4.1 Aerosol-cloud relationships in the PD

Following Quaas et al. (2009), the strength of aerosol-cloud interactions (ACI) is defined as the relative change in cloud properties with respect to the relative change in aerosol optical properties, and is calculated as:

$$\mathrm{ACI} = \frac{d\ln C}{d\ln A},$$

where $C$ is a cloud parameter (e.g., cloud droplet number concentration, cloud LWP, or cloud fraction), and $A$ is a proxy for column-integrated aerosol number concentrations. Quaas et al. (2009) used AOD as the proxy for column-integrated aerosol number concentration. Aerosol Index (AI), which is the product of AOD and Angstrom coefficient, has also been used in some previous studies to represent column-integrated aerosol number concentrations. Compared to AOD, AI is more representative of the column-integrated aerosol number concentrations since the Angstrom coefficient accounts for





ACPD
11, 3399–3459, 2011



the particle size with smaller Angstrom coefficients for larger size particles. Here both AOD and AI are used as proxies for the column-integrated aerosol number concentrations to calculate ACI in the MMF model for cloud droplet number concentrations, LWP, and cloud fraction, following the same approach as that used in Quaas et al. (2009). ACI is obtained by a linear regression between ln$C$ and ln$A$. Model output is sampled daily at 1:30 p.m. LT to match the MODIS Aqua equatorial crossing time. The model output is interpolated to a 2.5° × 2.5° regular longitude-latitude grid as in Quaas et al. (2009), to facilitate the direct comparison between the current study and Quaas et al. (2009). The regressions for the MMF and CAM5 simulations are performed separately for fourteen different ocean and land regions and four seasons as in Quaas et al. (2009). We compare the MMF results with those from the standard CAM5, and those from the observations and other model results in Quaas et al. (2009).

Figure 11 shows the mean sensitivities of cloud parameters to column aerosol properties for all seasons in both the land and ocean areas from the satellite data, and from the MMF and CAM5 simulations, with the error bars showing the variability among 6 land or 8 ocean regions and 4 seasons. Cloud-top droplet number concentration increases with increasing AOD in both models and satellite observations (Fig. 11a). Simulated slopes between cloud-top droplet number concentration and AOD are similar in the MMF and CAM5, with a slightly larger slope in the MMF, and are significantly larger than that in satellite observations. Quaas et al. (2009) showed that most global climate models overestimated the slope. Replacing AOD with AI in the MMF and CAM5 further increases the slope, which is consistent with McComiskey et al. (2009).

The slope between LWP and AOD is positive over land in the MMF model, consistent with those in satellite observations and CAM5, but the magnitude is larger in the MMF than in the satellite observations and in CAM5. In contrast, LWP and AOD over ocean are negatively correlated in the MMF, which is opposite to those in CAM5 and the MODIS retrievals. Replacing AOD with AI leads to larger negative/positive slope over ocean/land for the MMF. Both positive and negative correlations between LWP and AOD have been observed (Platnick et al., 2000; Coakley and Walsh, 2002; Kaufman





ACPD
11, 3399–3459, 2011



et al., 2005; Matsui et al., 2006). Using a global CRM with on-line aerosols, Suzuki et al. (2008) also obtained a negative correlation between LWP and AOD from a 8-day integration in July. The positive correlation between LWP and AOD is attributed to cloud lifetime effects or/and aerosol swelling effects in the high relative humidity regions surrounding clouds. The negative correlation between LWP and AOD can be attributed to rain wash-out effects (Suzuki et al., 2004), semi-direct effects (Hansen et al., 1997), or dynamical feedbacks such as enhanced entrainment of drier air or enhanced evaporation of the more numerous smaller cloud droplets in polluted clouds (Ackerman et al., 2004; Jiang et al., 2006). Our results suggest that the negative effect dominates over ocean while the positive effect dominates over land in the MMF model.

Simulated cloud fraction and AOD are negatively correlated in the MMF and CAM5, opposite to the correlation found in the satellite retrievals, though using AI instead of AOD leads to a slightly positive correlation over land in both models. The positive correlation in satellite data can be attributed to the swelling of aerosol particles near clouds, cloud lifetime effects, or the contamination in AOD retrievals by clouds. Quaas et al. (2010) showed that the positive correlation between cloud fraction and AOD in their model can largely be attributed to the aerosol swelling effects, and a negative correlation is found when dry AOD is used. The negative correlation between cloud fraction and AOD in CAM5 and the MMF may indicate the stronger scavenging effects of clouds on aerosols and/or less swelling effects of clouds on aerosols in both models. We noted that the MMF AOD is from the clear-sky CRM columns and therefore may be less susceptible to the swelling effects than CAM5 AOD.

### 4.2 Anthropogenic aerosol effects

#### 4.2.1 Anthropogenic aerosol effects in the MMF

As summarized in Table 2, simulated aerosol loadings have increased significantly since preindustrial time. Globally, sulfate, BC, POM, and SOA burdens increase by 133%, 133%, 55%, and 17%, respectively from the PI to PD. Dust and sea salt burden





ACPD
11, 3399–3459, 2011



are similar in both PI and PD simulations. The lifetimes of sulfate, SOA, dust and sea salt increase slightly from PI to PD, which may be caused in part by cloud lifetime effects (more aerosols lead to longer cloud lifetime, and therefore less efficient wet removal in PD than in PI), a positive feedback in aerosol indirect effects. On the other hand, the lifetimes of BC and POM decrease from PI to PD, which may be caused in part by enhanced sulfate coating on BC and POM and therefore enhanced wet removal of BC and POM in the PD.

Figure 12 shows the global distribution of changes in annual-mean cloud-top droplet number concentrations and cloud-top droplet effective radius between the PD and the PI simulations (PD–PI). Cloud-top droplet number concentrations increase from the PI to PD simulations over most regions, and increases in cloud-top droplet number concentrations are mainly located in the source regions of fossil fuel burning (e.g., more than 50 $cm^{-3}$ in Europe, East and South Asia) and biomass burning (e.g., more than 30 $cm^{-3}$ in Africa and South America), and downwind of the source regions (e.g., between 10–30 $cm^{-3}$ in the mid-latitude Pacific and the tropical Atlantic). Decreases in droplet number concentrations are simulated in some regions, such as Southeast United States, Central South America, and North Australia, which are caused by reduced biomass burning emissions from PI to PD (not shown). Cloud-top droplet effective radius decreases from the PI to PD simulations over most regions, by more than 1 µm over strongly polluted regions (e.g., East and South Asia) and more than 0.5 µm over many oceanic regions (e.g., the North Pacific). The spatial pattern of changes in droplet effective radius is consistent with the spatial pattern of changes in cloud-top droplet number concentrations (i.e., large increases in droplet number concentrations lead to large decreases in droplet effective radius).

Figure 13 shows the zonal distribution of changes in AOD, cloud liquid water path (LWP), cloud-top droplet effective radius (CDR), cloud-top droplet number concentrations (CDNC), shortwave cloud forcing (SWCF), and net total fluxes (shortwave + longwave) at the top of the atmosphere (FSNT + FLNT) between the PD and PI simulations. Increases in AOD from the anthropogenic aerosols are mainly located





ACPD
11, 3399–3459, 2011



north of 30° S, and peak in the NH mid-latitude with a value of about 0.04. Increases in cloud-top droplet number concentrations closely follow the changes in AOD, with a peak of about 40 $cm^{-3}$ in the NH mid-latitudes. Decreases in cloud-top droplet effective radius are larger over the NH mid-latitude, consistent with the large increases in cloud-top droplet number concentration, and also larger over the NH high latitudes, which can be explained by the large relative changes in cloud-top droplet number concentrations. Increases in LWP are large over the tropics and the NH mid-latitudes, which is consistent with the increases in cloud droplet number concentrations over these regions. On the other hand, changes in LWP in the NH subtropics and the latitude bands around 60° N are small though changes in cloud-top droplet number concentrations are large over these regions. Increases in the shortwave cloud forcing (in the absolute amount) are caused by both decreases in droplet effective radius and increases in LWP, while its changes follow more closely with changes in LWP than with changes in droplet effective radius (e.g., smaller changes in the NH subtropics, and around 60° N). Changes in net total fluxes at the top of the atmosphere are larger in the NH than in the SH.

The global mean changes from the PI to PD simulations are summarized in Table 3. Globally, anthropogenic aerosols lead to a 0.024 increase in clear-sky AOD, 24 $cm^{-3}$ increase in cloud-top droplet number concentrations, a 0.53 µm decrease in cloud-top droplet effective radius, and a 2.10 g $m^{-2}$ increase in LWP. A cooling of 0.77 W $m^{-2}$ in shortwave cloud forcing is simulated, which results from the decreases in cloud droplet effective radius and increases in liquid water path. As expected, simulated longwave cloud forcing has little change between the PD and PI simulations since aerosol effects on ice clouds are not accounted for in this version of the MMF model. Simulated total aerosol effect on the shortwave fluxes at the top of the atmosphere is −1.31 W $m^{-2}$. Aerosol effect in the clear-sky (assuming entirely clear grid boxes) is −0.54 W $m^{-2}$. Simulated aerosol effect on the net total fluxes (shortwave + longwave) is −1.05 W $m^{-2}$, with a longwave contribution of 0.26 W $m^{-2}$. The longwave warming of 0.26 W $m^{-2}$ is mainly from the contribution in the clear sky, which is caused in part by cooling over land surface (surface temperature over land decreases by 0.34 K) and therefore less





ACPD
11, 3399–3459, 2011



thermal emission from land.

#### 4.2.2 Comparison with CAM5

In the standard version of CAM5, simulated PI to PD changes in shortwave cloud forcing, changes in longwave cloud forcing, aerosol direct effects in the clear sky (assuming entirely clear grid boxes), and total aerosol effects are −1.79, 0.37, −0.45, and −1.66 W m$^{-2}$, respectively. A larger clear-sky direct effect in the MMF than in CAM5 (−0.54 W m$^{-2}$ in the MMF vs. −0.45 W m$^{-2}$ in CAM5) can be explained in part by the larger increase in sulfate burden from PI to PD in the MMF (0.60 Tg S) than in CAM5 (0.36 Tg S). We also noted that aerosol water uptake in the MMF is calculated at each CRM grid cell with a CRM-scale relative humidity, while aerosol water uptake in CAM5 is calculated at each GCM grid cell with a GCM-grid scale clear-sky relative humidity. This may be another reason why the MMF simulates the larger clear-sky direct effects, as previous studies (Haywood et al., 1997) showed that including subgrid variations in the relative humidity can lead to larger aerosol direct effects because of the nonlinear dependence of aerosol water uptake on relative humidity.

The simulated change in shortwave cloud forcing in the MMF (−0.77 W m$^{-2}$) is much smaller than that in CAM5 (−1.79 W m$^{-2}$), despite the fact that changes in AOD and cloud-top droplet effective radius from anthropogenic aerosols in the MMF are slightly larger than those in CAM5 (Table 3 and Figs. 12, 13). For example, the global, annual mean change in cloud-top droplet effective radius is −0.53 µm in the MMF simulations, compared with −0.45 µm in the CAM5 simulations (Table 3 and Fig. 12).

On the other hand, the smaller change in shortwave cloud forcing in the MMF is consistent with its smaller change in liquid water path (LWP) between the PI and PD simulations. Globally, an increase of 3.9% in LWP from PI to PD is simulated in the MMF, which is about one-fourth of the change of 15.6% in LWP in large-scale clouds (and about half of the change of 8.8% in total LWP) in CAM5. Regionally, in CAM5 the LWP in large-scale clouds increases by more than 50% over many continental regions with strong anthropogenic emissions (e.g., East Asia, South Asia, the Maritime





ACPD
11, 3399–3459, 2011



Continent, and Europe) and increases by more than 20% over some oceanic regions such as the North Pacific Ocean (Fig. 14). In contrast, the increase in LWP in the MMF is much weaker, less than 30% over most continental regions, and less than 10% over most oceanic regions. The scatter plots of the relative change in LWP and in shortwave cloud forcing shown in Fig. 15 further demonstrate that the larger change in LWP in CAM5 leads to the larger change in shortwave clouds forcing. Zonal distributions of aerosol indirect effects in Fig. 13 also suggest that the large differences in simulated aerosol indirect effects between the MMF and CAM5 occur over the regions where the difference in changes in LWP are larger such as the NH subtropics (compare Fig. 13b and e).

To further examine how clouds with different LWP may respond differently to anthropogenic aerosols, Fig. 16 shows the probability density function (PDF) of in-cloud LWP over the globe in the PD simulations and the relative changes in the PDF of in-cloud LWP from the PI to PD simulations in both the MMF and CAM5. Model output (34 months data for the MMF and 4 years data for CAM5) are sampled daily at 1:30 p.m. LT. For the MMF model, the PDF of LWP is calculated from in-cloud LWP at each CRM column (Fig. 16b and solid line in Fig. 16a) and at each GCM column (Fig. 16c and dotted line in Fig. 16a). For CAM5, the PDF of LWP is calculated from in-cloud LWP at each GCM column (Fig. 16d and dash-dot line in Fig. 16a). The in-cloud LWP in CAM5 is derived from grid-mean LWP, and liquid cloud cover that is calculated based on the same maximum/random cloud overlap assumption used in the radiative transfer calculation in CAM5. The PDFs of LWP calculated from in-cloud LWP at each GCM column in both the MMF and CAM5 (Fig. 16c and d) are weighted by cloud cover. In-cloud LWP in CAM5 includes contribution from large-scale clouds only, while in-cloud LWP in the MMF includes contributions from both large-scale and convective clouds. The PDFs of LWP in PD show that the frequency of occurrence of LWP decreases with increasing LWP and that clouds with LWP larger than 200 $\mathrm{g\,m^{-2}}$ occur more often in the MMF than in the CAM5 (Fig. 16a).





ACPD
11, 3399–3459, 2011



The relative changes in the PDF of LWP (green lines in Fig. 16b–d) show that cloud fraction of thin clouds decreases and that cloud fraction of thick clouds increases in both the MMF and CAM5 from the PI to PD simulations (relative changes in the frequency of occurrence of a given LWP bin is equivalent to relative changes in cloud fraction for that given LWP bin). It is also evident in Fig. 16b–d that cloud fraction increases in thick clouds accelerate with increasing LWP bins. For example, in the MMF, cloud fraction decreases for clouds with in-cloud LWP less than 80 g m$^{-2}$ and increases otherwise. For the smallest LWP bins, the decreases in cloud fraction can reach as high as 2%, while the increase in cloud fraction can be larger than 10% for clouds with LWP larger than 1000 g m$^{-2}$. When the PDF of LWP is calculated from the in-cloud LWP at each GCM column in the MMF (Fig. 16c), the difference between thin and thick clouds is even larger. The decreases in cloud fraction can reach as high as 4% for the smallest LWP bins, while the increase in cloud fraction can be larger than 10% for clouds with LWP larger than 350 g m$^{-2}$.

The different responses of thin and thick cloud LWP to anthropogenic aerosol perturbations can be explained in part by cloud lifetime effects. Thick clouds are more likely to precipitate and therefore their LWP are more susceptible to anthropogenic aerosol perturbations. The accelerating increase in cloud fraction for thick clouds with increasing LWP may partly result from the autoconversion scheme used in the models, which is based on Khairoutdinov and Kogan (2000). The autoconversion rate in Khairoutdinov and Kogan scheme has a strong dependence on liquid water content ($q_c^{2.47}$), which leads to a strong dependence of the relative autoconversion rate (the autoconversion rate divided by liquid water content) on liquid water content ($q_c^{1.47}$) and therefore larger relative increases in cloud fraction for clouds with larger LWP. On the other hand, thin clouds are less likely precipitating and their LWPs are therefore less susceptible to anthropogenic aerosol perturbations. Other factors, such as semi-direct effects, and dynamical feedbacks (e.g., entrainment drying, Ackerman et al., 2004) can even lead to a decrease in cloud fraction for these thin clouds.





ACPD
11, 3399–3459, 2011



Figure 16 shows that LWP changes are much larger in CAM5 than in the MMF. In CAM5, cloud fraction increases for clouds with in-cloud LWP less than 50 g m$^{-2}$, and decreases otherwise. For the smallest LWP bins, the decrease in cloud cover is similar to that in the MMF, and can reach as high as 4%. On the other hand, for the larger LWP bins in CAM5, increase in cloud fraction is larger than 20% for clouds with LWP lager than 200 g m$^{-2}$, and is larger than 50% for clouds with LWP larger than 400 g m$^{-2}$. The larger response in LWP in CAM5 can also be seen in the changes in the cumulative PDF of LWP (blue lines in Fig. 16b–d). In the MMF, total cloud fraction for clouds with LWP less than 300 g m$^{-2}$ decreases, and total cloud fraction for all LWP bins only slightly increases. In CAM5, total cloud fraction for clouds with LWP less than 70 g m$^{-2}$ decreases, and total cloud fraction for all LWP bins increases by about 5%.

The cumulative LWP (red lines in Fig. 16b–d) shows that in-cloud LWP increases by less 4% in the MMF while it increases by about 10% in CAM5 (for a given LWP bin, the cumulative LWP is the in-cloud LWP averaged from the smallest LWP bin to the given LWP bin). These results are consistent with the grid-mean LWP changes shown in Fig. 14. Changes in grid-mean LWP come from both changes in cloud fraction (the cumulative PDF) and in in-cloud LWP (the cumulative LWP). Figure 16 shows that the 3.9% increase in grid-mean LWP in the MMF is mainly from the changes in in-cloud LWP, while the 15.6% increase in large-scale LWP in CAM5 is from about 5% change in cloud fraction, and 10% change in in-cloud LWP.

Comparing changes in LWP (Fig. 14) with changes in CCN concentrations (Fig. 9), it is clear that changes in LWP in large-scale clouds in CAM5 closely follow changes in CCN concentrations. Large-scale LWP increases significantly over regions with large increases in CCN concentrations, such as East Asia and the Maritime Continent. Compared with CAM5, increases in CCN concentrations in the MMF are weaker, which is consistent with the weaker increase in LWP in the MMF. The scatter plot of the relative changes in CCN concentrations from the PD to PI simulations in both the MMF and CAM5 (Fig. 17a) shows that the relative changes in CCN concentrations in CAM5 are about 35% larger than that in the MMF. The larger relative increases in CCN





ACPD
11, 3399–3459, 2011



concentrations in CAM5 than in the MMF are consistent with the changes in aerosol lifetimes between the PD and PI simulations (Table 2). The lifetime of sulfate aerosol is almost the same in the PD and PI simulations in the MMF, but increases by 12% from the PI to PD simulations in CAM5. The lifetime of BC decreases by 7% from the PI to PD simulations in the MMF, while it increases by 9% in CAM5. The large increase in sulfate and BC lifetimes in CAM5 from the PI to PD simulations can be explained in part by the positive feedback in aerosol indirect effects due to cloud lifetime effects (more aerosols lead to longer cloud lifetime and therefore less wet scavenging, which in turn increases CCN concentrations). Our results indicate that this positive feedback induced by cloud lifetime effects is stronger in CAM5 than in the MMF, and can partly explain the stronger changes in shortwave cloud forcing in CAM5 due to anthropogenic aerosol perturbations.

Comparing changes in LWP (Fig. 14) with changes in CCN concentrations (Fig. 9), it is also clear that the MMF produces more regions with negative response in LWP to anthropogenic aerosols than CAM5. For example, though CCN concentrations increase significantly from the PI to PD simulations over South China, LWP changes little or even decreases in the MMF, while it increases significantly in CAM5. Figure 16 also shows that negative changes in cloud fraction extend to thicker clouds in the MMF than in CAM5. This indicates that factors other than the differences in the relative changes in CCN concentrations are also important in causing the smaller increase in LWP in the MMF model.

Figure 17b and c compare the relative changes in CCN concentrations with the relative changes in LWP in both the MMF and CAM5, respectively. It is clear that the much smaller increase in LWP in the MMF is caused primarily by the much smaller response in LWP to a given change in CCN. The slope between the relative change in LWP and the relative change in CCN from the linear regression is 0.11 in the MMF, which is only about one-third of that in CAM5 (0.30). As implemented in most global climate models, increases in cloud droplet number concentration due to the addition of anthropogenic aerosol particles leads to less efficient coalescence and collection among





ACPD
11, 3399–3459, 2011



cloud droplets, which results in less precipitation, larger LWPs and longer cloud lifetimes (Albrecht, 1989). However, ship track studies show that anthropogenic aerosols can lead to less liquid water (Platnick et al., 2000; Coakley and Walsh, 2002), and satellite studies show both decreases and increases in LWP with increasing aerosols (Kaufman et al., 2005; Matsui et al., 2006). CRM studies have suggested that LWP can either increase or decrease with increasing aerosols, depending on the meteorological conditions (Ackerman et al., 2004; Jiang et al., 2006; Guo et al., 2007; Xue et al., 2008; Small et al., 2009). The decreasing LWP with increasing aerosols can be attributed to enhanced entrainment of dry air or enhanced evaporation of the more numerous smaller cloud droplets in polluted clouds. Stevens and Feingold (2009) further argued that the aerosol-cloud interactions work in a buffered system, and cloud lifetime effects as hypothesized in the system in isolation may be canceled or compensated for by opposing changes when the system is viewed as a whole. Most conventional global climate models implemented cloud lifetime effects through their large-scale cloud parameterization and are not able to account for the sophisticated balance between different factors, and hence may overestimate cloud lifetime effects. Compared with CAM5, the smaller increase in LWP in the MMF model is more consistent with the observations and with CRM studies.

#### 4.2.3 Comparison with other studies

The smaller increase in LWP in the MMF model is consistent with Lohmann (2008), who showed a slightly smaller response in LWP in a version of the ECHAM including aerosol effects on convective clouds using cumulus parameterization (8.2%) compared to a version of the ECHAM without aerosol effects on convective clouds (9.7%) though conventional cloud parameterizations are used for both stratiform and convective clouds. In Lohmann (2008), the total aerosol effect decreases slightly from $-1.9\,\mathrm{W\,m^{-2}}$ without aerosol effects on convective clouds to $-1.7\,\mathrm{W\,m^{-2}}$ with aerosol effects on convective clouds. Our results are also consistent with the GISS model results in Menon and Rotstayn (2006), which simulates a smaller increase in LWP due to anthropogenic aerosols





ACPD
11, 3399–3459, 2011



when aerosol effects on convective clouds are included. In contrast, the CSIRO model in Menon and Rotstayn (2006) simulates a larger increase in LWP when aerosol effects on convective clouds are included. Menon and Rotstayn (2006) attributed the different responses in the CSIRO and GISS models to the different treatment of detrained condensate in their cumulus parameterizations, which includes different treatments on how to partition convective condensate into precipitation and detrained condensate, and on how to treat detrained cloud condensate (instantly evaporate in CSIRO, and is added directly as anvil clouds in GISS). It is not clear in Menon and Rotstayn (2006) why these differences lead to different responses in liquid water path to anthropogenic aerosols in the two models.

The estimated shortwave cloudy-sky forcing, calculated from subtracting aerosol effects in the clear sky weighted by the clear-sky fraction from the total shortwave forcing, is $-1.07\,W\,m^{-2}$, which is at the low end of the estimates of global aerosol-climate models included in a recent AeroCom indirect effect model intercomparison study (Quaas et al., 2009). The estimated shortwave cloudy-sky forcing in Quaas et al. (2009) range from $-0.27$ to $-1.87\,W\,m^{-2}$ with a mean value of $-1.15\,W\,m^{-2}$ though none of the participated AeroCom models included aerosol indirect effects on convective clouds. The AeroCom models that produced small shortwave cloudy-sky forcing typically set a larger lower limit for simulated droplet number concentrations ranging from 20 to $40\,cm^{-3}$. It has been shown in several previous studies (Ghan et al., 2001; Hoose et al., 2009; Wang and Penner, 2009) that the larger lower limits usually lead to smaller aerosol indirect effects. The CRM in the MMF model does not include any lower limit on simulated cloud droplet number concentrations, the same as CAM5 and several other models in Quaas et al. (2009) that generally produced larger shortwave cloudy-sky forcing.

The AeroCom models that produced low shortwave cloud-sky forcing also typically have a weak dependence of autoconversion rate on cloud droplet number concentrations. For example, the smallest forcing in the AeroCOM models ($-0.27\,W\,m^{-2}$) is from a model that has an autoconversion scheme independent of cloud droplet number





ACPD
11, 3399–3459, 2011



concentrations. The AeroCom models that used the same Khairoutdinov and Kogan (2000) scheme as in the MMF and CAM5, which gives the strongest dependence of autoconversion rate on cloud droplet number concentrations ($N_d^{-1.79}$) among the AeroCom models, generally produce large changes in shortwave cloud forcing. It must be noted that the Khairoutdinov and Kogan scheme is applied at each CRM grid point with a grid spacing of 4 km in the MMF model, while it is applied at each GCM grid point with a grid spacing of several hundred kilometers in CAM5 and other conventional GCMs included in the AeroCom study. To take account of the strongly non-linear dependence of autoconversion rate on subgrid cloud liquid water, most conventional GCMs either derive the autoconversion rate based on an assumed probability distribution of subgrid cloud liquid water or simply tune the autoconversion rate to produce reasonable results (Pincus and Klein, 2000; Rotstayn, 2000; Larson et al., 2001; Morrison and Gettelman, 2008). Subgrid variations in cloud droplet number concentrations are typically neglected in these GCMs. For example, CAM5 assumes a gamma distribution of subgrid cloud liquid water content with a relative variance of 2 and neglects the subgrid variation in cloud droplet number concentrations, which results in a scaling factor of about 2 applied to the autoconversion rate calculated based on the GCM-scale in-cloud liquid water content and cloud droplet number concentration (Morrison and Gettelman, 2008). Neglecting the subgrid variation in cloud droplet number concentrations may bias the autoconversion rate, since cloud droplet number concentrations may correlate with cloud water content on the subgrid scale (e.g., larger cloud water may be well associated with larger droplet number concentrations). It is not clear how the differences in scale may play a role on the differences in aerosol indirect effects between the MMF model and conventional GCMs.

Aerosol effects in the clear-sky (assuming entirely clear grid boxes) in Quaas et al. (2009) range from $-0.17$ to $-1.76\,\mathrm{W\,m^{-2}}$, with a mean value of $-0.68\,\mathrm{W\,m^{-2}}$. Our estimated aerosol effect in the clear-sky (assuming entirely clear grid boxes) is $-0.54\,\mathrm{W\,m^{-2}}$, and is in the range of the AeroCOM model estimates in Quaas et al. (2009). The clear-sky forcing efficiency (forcing per unit anthropogenic AOD) is





ACPD
11, 3399–3459, 2011



$-22.5\,W\,m^{-2}$ per unit anthropogenic AOD, which is in the range of the estimates in the AeroCOM study (from −2.78 to −30.71). The clear-sly forcing efficiency in this study is also close to the results in an early AeroCom intercomparison study of Schulz et al. (2006) that focused on aerosol direct effects only, which range from −10 to $33\,W\,m^{-2}$ per unit anthropogenic AOD, with a mean of $-23\,W\,m^{-2}$ per unit anthropogenic AOD.

Our estimated total aerosol effect on the shortwave radiative fluxes at the top of the atmosphere is $-1.34\,W\,m^{-2}$, which falls well within the model results of Quaas et al. (2009) that range from $-0.50$ to $-2.56\,W\,m^{-2}$, with a mean value of $-1.57\,W\,m^{-2}$. The estimated total aerosol effect on the net radiative fluxes at the top of the atmosphere is $-1.05\,W\,m^{-2}$, which is close to the inverse estimate of $-1.1 \pm 0.4\,W\,m^{-2}$ ($1\sigma$) based on the examination of the Earth's energy balance in Murphy et al. (2009).

## 5 Summary

In this study, we have evaluated model fields in a multi-scale aerosol-climate model and examined aerosol effects on clouds and climate. The PNNL-MMF multi-scale aerosol-climate model is an extension of the Colorado State University (CSU) multi-scale modeling framework (MMF) model (Khairoutdinov et al., 2005, 2008; Tao et al., 2009) and consists of three components (Wang et al., 2010). The global climate model (GCM) component is NCAR CAM5 and includes a modal aerosol treatment that uses several log-normal modes to represent aerosol size distributions. The cloud resolving model (CRM) component is SAM, which has a two-moment microphysics scheme and predicts both hydrometeor mass and number mixing ratios. The CRM is embedded in each GCM grid column and replaces the conventional parameterizations of convective and large-scale clouds, which permits the explicit simulation of convective clouds. The third component of this multi-scale aerosol-climate model is the Explicit-Cloud-Parameterized-Pollutant approach, which uses cloud statistics diagnosed from the CRM component of the MMF model to drive the aerosol and trace gas processing by clouds. This multi-scale aerosol-climate model allows us to explicitly simulate





ACPD
11, 3399–3459, 2011



aerosol/cloud interactions in both stratiform and convective clouds. Wang et al. (2010) showed that this model simulates aerosol fields in reasonable agreement with observations.

Simulated model fields, including liquid water path (LWP), ice water path, cloud fraction, shortwave and longwave cloud forcing, precipitation and water vapor are in reasonable agreement with observations. However, the model underestimates cloud fraction, especially for low clouds, and overestimates precipitation rate over the tropical ocean and underestimates precipitation over the mid-latitudes. The model performs quantitatively similarly to the previous version of the MMF model in terms of simulated cloud fraction and precipitation, and the two-moment cloud microphysics coupled with a modal aerosol treatment provides little help in reducing biases in these fields. Simulated cloud-top droplet number concentrations are in reasonable agreement with satellite observations, with a larger droplet number concentration over land than over ocean, and over the NH than over the SH. A large fraction of total ice water mass is from snow, and including the radiative effects of snow significantly increases both shortwave and longwave cloud forcing. Simulated sulfate, BC, POM and SOA burdens are larger in the MMF than in CAM5, which can be explained in part by the smaller wet removal rate in the MMF. Simulated aerosol size distributions in the marine boundary layer in the MMF are similar with those in CAM5, and agree slightly better with observations. BC concentrations in the polar regions in the MMF are much higher than that in CAM5 and agree better with observations in terms of both magnitude and seasonal cycle.

Cloud-top droplet number concentration (CDNC) increases with increasing AOD in the MMF model, which is consistent with satellite data and other model studies, though the slope between ln(CDNC) and ln(AOD) in the MMF is overestimated compared with satellite data, which is also a common feature in many conventional aerosol-climate models including CAM5. Cloud LWP increases with increasing AOD over land in the MMF model, with a larger slope between ln(LWP) and ln(AOD) in the MMF than in CAM5 and satellite data. In contrast, cloud LWP decreases with increasing AOD over





ACPD
11, 3399–3459, 2011



ocean, which is opposite to CAM5 and many other aerosol-climate models. Both positive and negative correlation between LWP and AOD have been observed, and simulated in CRM models. Simulated cloud fraction and AOD are negatively correlated in the MMF, similar to CAM5, but opposite to many other conventional aerosol-climate models, although cloud fraction and AI are slightly positively correlated in the MMF model. The negative correlation may suggest stronger scavenging effects of clouds and less swelling of aerosols near clouds in the MMF and CAM5.

The simulated change of $-0.77\,\mathrm{W\,m^{-2}}$ in shortwave cloud forcing in the MMF is less than half of that in CAM5 ($-1.79\,\mathrm{W\,m^{-2}}$), though decreases in simulated cloud-top droplet effective radius from anthropogenic aerosols are slightly larger in the MMF than in CAM5 ($-0.53\,\mu\mathrm{m}$ vs. $-0.44\,\mu\mathrm{m}$). The simulated change in cloudy-sky forcing in the MMF is also at the low end of the estimates of global climate models included in a recent AeroCom aerosol indirect effect intercomparison study (Quaas et al., 2009). The smaller forcing in the MMF model is attributed to the much smaller increase in LWP from anthropogenic aerosols (3.9% in the MMF, compared with 15.6% increase in LWP in large-scale clouds in CAM5). The much smaller increase in LWP in the MMF can be explained by the much smaller response in LWP to a given change in CCN concentrations in the MMF, which is only about one-third of that in CAM5, and, to a lesser extent, by the smaller relative increase in CCN concentrations from the PI to the PD simulations in the MMF, which is about 74% of that in CAM5. The smaller relative increase in CCN concentrations in the MMF is caused in part by the smaller positive feedback between aerosols and clouds due to cloud lifetime effects. The smaller response in LWP in the MMF model is consistent with observations and with CRM studies, and may indicate that aerosol indirect effects simulated in conventional global climate models are overestimated. The simulated total aerosol effects on the net radiative flux is $-1.05\,\mathrm{W\,m^{-2}}$, which is close to the inverse estimate of $-1.1 \pm 0.4\,\mathrm{W\,m^{-2}}$ ($1\sigma$) based on the examination of the Earth's energy balance in Murphy et al. (2009).

Further improvements in the representation of ice nucleation and low clouds are needed. In this study, ice nucleation in the MMF model is not directly related to aerosol





ACPD
11, 3399–3459, 2011



particles, while in CAM5, aerosol indirect effects on ice clouds produces a warming. Including aerosol effects on ice clouds in the MMF therefore may lead to an even smaller total aerosol effect. The CRM in this study also lacks a high-order turbulence scheme, and including such a scheme could improve the simulation of lower level clouds in the MMF model. These limitations will be addressed in future studies.

*Acknowledgements.* This work is supported by the NASA Interdisciplinary Science Program under grant NNX07AI56G and by the US Department of Energy, Office of Science, Atmospheric System Research program and Scientific Discovery through Advanced Computing (SciDAC) program. The Pacific Northwest National Laboratory (PNNL) is operated for the DOE by Battelle Memorial Institute under contract DE-AC06-76RLO 1830. We thank Duli Chand for his internal review and constructive comments. We are also grateful to Johannes Quaas for providing scripts to examine the aerosol/cloud relationships in models and for satellite data used in Figs. 6 and 11.

## References

Abdul-Razzak, H. and Ghan, S. J.: A parameterization of aerosol activation – 2. multiple aerosol types, J. Geophys. Res., 105, 6837–6844, 2000.

Ackerman, A. S., Kirkpatrick, M. P., Stevens, D. E., and Toon, O. B.: The impact of humidity above stratiform clouds on indirect aerosol climate forcing, Nature, 432, 1014–1017, doi:10.1038/Nature03174, 2004.

Albrecht, B. A.: Aerosols, cloud microphysics, and fractional cloudiness, Science, 245, 1227–1230, 1989.

Bigg, E. K.: The supercooling of water, P. Phys. Soc. Lond. B, 66, 688–694, 1953.

Bodhaine, B. A.: Aerosol absorption-measurements at Barrow, Mauna-Loa and the South-Pole, J. Geophys. Res., 100, 8967–8975, 1995.

Coakley, J. A. and Walsh, C. D.: Limits to the aerosol indirect radiative effect derived from observations of ship tracks, J. Atmos. Sci., 59, 668–680, 2002.

Cooper, W. A.: Ice initiation in natural clouds, in: Precipitation Enhancement – a Scientific Challenge, Meteor. Monogr., Amer. Meteor. Soc., Boston, MA, USA, 29–32, 1986.





ACPD
11, 3399–3459, 2011



Del Genio, A. D., Kovari, W., Yao, M. S., and Jonas, J.: Cumulus microphysics and climate sensitivity, J. Climate, 18, 2376–2387, 2005.
Dentener, F., Kinne, S., Bond, T., Boucher, O., Cofala, J., Generoso, S., Ginoux, P., Gong, S., Hoelzemann, J. J., Ito, A., Marelli, L., Penner, J. E., Putaud, J.-P., Textor, C., Schulz, M., van der Werf, G. R., and Wilson, J.: Emissions of primary aerosol and precursor gases in the years 2000 and 1750 prescribed data-sets for AeroCom, Atmos. Chem. Phys., 6, 4321–4344, doi:10.5194/acp-6-4321-2006, 2006.
Emanuel, K. A. and Zivkovic-Rothman, M.: Development and evaluation of a convection scheme for use in climate models, J. Atmos. Sci., 56, 1766–1782, 1999.
Ferraro, R. R., Weng, F. Z., Grody, N. C., and Basist, A.: An eight-year (1987–1994) time series of rainfall, clouds, water vapor, snow cover, and sea ice derived from SSM/I measurements, B. Am. Meteorol. Soc., 77, 891–905, 1996.
Forster, P., Ramaswamy, V., Artaxo, P., Berntsen, T., Betts, R., Fahey, D. W., Haywood, J., Lean, J., Lowe, D. C., Myhre, G., Nganga, J., Prinn, R., Raga, G., Schulz, M., and Dorland, R. V.: Changes in Atmospheric Constituents and in Radiative Forcing, in: Climate Change 2007: The Physical Science Basis. Contribution of Working Group I to the Fourth Assessment Report of the Intergovernmental Panel on Climate Change, edited by: Solomon, S., Qin, D., Manning, M., Chen, Z., Marquis, M., Averyt, K. B., Tignor, M., and Miller, H. L., Cambridge University Press, Cambridge and New York, NY, 2007.
Gettelman, A., Liu, X., Ghan, S. J., Morrison, H., Park, S., Conley, A. J., Klein, S. A., Boyle, J., Mitchell, D. L., and Li, J. L. F.: Global simulations of ice nucleation and ice supersaturation with an improved cloud scheme in the community atmosphere model, J. Geophys. Res., 115, D18216, doi:10.1029/2009jd013797, 2010.
Ghan, S. J. and Zaveri, R. A.: Parameterization of optical properties for hydrated internally mixed aerosol, J. Geophys. Res., 112, D10201, doi:10.1029/2006jd007927, 2007.
Ghan, S. J., Easter, R. C., Chapman, E. G., Abdul-Razzak, H., Zhang, Y., Leung, L. R., Laulainen, N. S., Saylor, R. D., and Zaveri, R. A.: A physically based estimate of radiative forcing by anthropogenic sulfate aerosol, J. Geophys. Res., 106, 5279–5293, 2001.
Greenwald, T. J., Stephens, G. L., Vonderhaar, T. H., and Jackson, D. L.: A physical retrieval of cloud liquid water over the global oceans using special sensor microwave imager (SSM/I) observations, J. Geophys. Res., 98, 18471–18488, 1993.
Guo, H., Penner, J. E., Herzog, M., and Pawlowska, H.: Examination of the aerosol indirect effect under contrasting environments during the ACE-2 experiment, Atmos. Chem. Phys.,





ACPD
11, 3399–3459, 2011



7, 535–548, doi:10.5194/acp-7-535-2007, 2007.
Gustafson, W. I., Berg, L. K., Easter, R. C., and Ghan, S. J.: The explicit-cloud parameterized-pollutant hybrid approach for aerosol-cloud interactions in multiscale modeling framework models: tracer transport results, Environ. Res. Lett., 3, 025005, doi:10.1088/1748-9326/3/2/025005, 2008.
Han, Q. Y., Rossow, W. B., and Lacis, A. A.: Near-global survey of effective droplet radii in liquid water clouds using ISCCP data, J. Climate, 7, 465–497, 1994.
Han, Q. Y., Rossow, W. B., Chou, J., and Welch, R. M.: Global variation of column droplet concentration in low-level clouds, Geophys. Res. Lett., 25, 1419–1422, 1998.
Hansen, J., Sato, M., and Ruedy, R.: Radiative forcing and climate response, J. Geophys. Res., 102, 6831–6864, 1997.
Haywood, J. M., Ramaswamy, V., and Donner, L. J.: A limited-area-model case study of the effects of sub-grid scale variations in relative humidity and cloud upon the direct radiative forcing of sulfate aerosol, Geophys. Res. Lett., 24, 143–146, 1997.
Heintzenberg, J., Covert, D. C., and Van Dingenen, R.: Size distribution and chemical composition of marine aerosols: a compilation and review, Tellus B, 52, 1104–1122, 2000.
Hoose, C., Kristjansson, J. E., Iversen, T., Kirkevag, A., Seland, O., and Gettelman, A.: Constraining cloud droplet number concentration in GCMs suppresses the aerosol indirect effect, Geophys. Res. Lett., 36, L12807, doi:10.1029/2009gl038568, 2009.
Hopper, J. F., Worthy, D. E. J., Barrie, L. A., and Trivett, N. B. A.: Atmospheric observations of aerosol black carbon, carbon-dioxide, and methane in the high Arctic, Atmos. Environ., 28, 3047–3054, 1994.
Horowitz, L. W., Walters, S., Mauzerall, D. L., Emmons, L. K., Rasch, P. J., Granier, C., Tie, X. X., Lamarque, J. F., Schultz, M. G., Tyndall, G. S., Orlando, J. J., and Brasseur, G. P.: A global simulation of tropospheric ozone and related tracers: description and evaluation of MOZART, version 2, J. Geophys. Res., 108, 4784, doi:10.1029/2002jd002853, 2003.
Iacono, M. J., Delamere, J. S., Mlawer, E. J., and Clough, S. A.: Evaluation of upper tropospheric water vapor in the NCAR Community Climate Model (CCM3) using modeled and observed HIRS radiances, J. Geophys. Res., 108, 4037, doi:10.1029/2002jd002539, 2003.
Iacono, M. J., Delamere, J. S., Mlawer, E. J., Shephard, M. W., Clough, S. A., and Collins, W. D.: Radiative forcing by long-lived greenhouse gases: calculations with the AER radiative transfer models, J. Geophys. Res., 113, D13103, doi:10.1029/2008jd009944, 2008.
IPCC: Climate Change 2007: The Physical Science Basis. Contribution of Working Group I to





ACPD
11, 3399–3459, 2011



the Fourth Assessment Report of the Intergovernmental Panel on Climate Change, edited by: Solomon, S., Qin, D., Manning, M., Chen, Z., Marquis, M., Averyt, K. B., Tignor, M., and Miller, H. L., Cambridge University Press, Cambridge, UK and New York, NY, USA, 996 pp., 2007.

Jiang, H. L., Xue, H. W., Teller, A., Feingold, G., and Levin, Z.: Aerosol effects on the lifetime of shallow cumulus, Geophys. Res. Lett., 33, L14806, doi:10.1029/2006gl026024, 2006.

Kaufman, Y. J., Koren, I., Remer, L. A., Rosenfeld, D., and Rudich, Y.: The effect of smoke, dust, and pollution aerosol on shallow cloud development over the Atlantic Ocean, Proc. Natl. Acad. Sci. USA, 102, 11207–11212, doi:10.1073/Pnas.0505191102, 2005.

Khairoutdinov, M. and Kogan, Y.: A new cloud physics parameterization in a large-eddy simulation model of marine stratocumulus, Mon. Weather Rev., 128, 229–243, 2000.

Khairoutdinov, M. F. and Randall, D. A.: A cloud resolving model as a cloud parameterization in the NCAR community climate system model: preliminary results, Geophys. Res. Lett., 28, 3617–3620, 2001.

Khairoutdinov, M. F. and Randall, D. A.: Cloud resolving modeling of the ARM summer 1997 IOP: model formulation, results, uncertainties, and sensitivities, J. Atmos. Sci., 60, 607–625, 2003.

Khairoutdinov, M., Randall, D., and DeMott, C.: Simulations of the atmospheric general circulation using a cloud-resolving model as a superparameterization of physical processes, J. Atmos. Sci., 62, 2136–2154, 2005.

Khairoutdinov, M., DeMott, C., and Randall, D.: Evaluation of the simulated interannual and subseasonal variability in an AMIP-Style simulation using the CSU multiscale modeling framework, J. Climate, 21, 413–431, doi:10.1175/2007jcli1630.1, 2008.

Kiehl, J. T. and Trenberth, K. E.: Earth's annual global mean energy budget, B. Am. Meteorol. Soc., 78, 197–208, 1997.

Kinne, S., Schulz, M., Textor, C., Guibert, S., Balkanski, Y., Bauer, S. E., Berntsen, T., Berglen, T. F., Boucher, O., Chin, M., Collins, W., Dentener, F., Diehl, T., Easter, R., Feichter, J., Fillmore, D., Ghan, S., Ginoux, P., Gong, S., Grini, A., Hendricks, J., Herzog, M., Horowitz, L., Isaksen, I., Iversen, T., Kirkevåg, A., Kloster, S., Koch, D., Kristjansson, J. E., Krol, M., Lauer, A., Lamarque, J. F., Lesins, G., Liu, X., Lohmann, U., Montanaro, V., Myhre, G., Penner, J., Pitari, G., Reddy, S., Seland, O., Stier, P., Takemura, T., and Tie, X.: An AeroCom initial assessment – optical properties in aerosol component modules of global models, Atmos. Chem. Phys., 6, 1815–1834, doi:10.5194/acp-6-1815-2006, 2006.





ACPD
11, 3399–3459, 2011



Lamarque, J.-F., Bond, T. C., Eyring, V., Granier, C., Heil, A., Klimont, Z., Lee, D., Liousse, C., Mieville, A., Owen, B., Schultz, M. G., Shindell, D., Smith, S. J., Stehfest, E., Van Aardenne, J., Cooper, O. R., Kainuma, M., Mahowald, N., McConnell, J. R., Naik, V., Riahi, K., and van Vuuren, D. P.: Historical (1850–2000) gridded anthropogenic and biomass burning emissions of reactive gases and aerosols: methodology and application, Atmos. Chem. Phys., 10, 7017–7039, doi:10.5194/acp-10-7017-2010, 2010.

Larson, V. E., Wood, R., Field, P. R., Golaz, J. C., Vonder Haar, T. H., and Cotton, W. R.: Systematic biases in the microphysics and thermodynamics of numerical models that ignore subgrid-scale variability, J. Atmos. Sci., 58, 1117–1128, 2001.

Lohmann, U.: Global anthropogenic aerosol effects on convective clouds in ECHAM5-HAM, Atmos. Chem. Phys., 8, 2115–2131, doi:10.5194/acp-8-2115-2008, 2008.

Lohmann, U., Spichtinger, P., Jess, S., Peter, T., and Smit, H.: Cirrus cloud formation and ice supersaturated regions in a global climate model, Environ. Res. Lett., 3, 045022, doi:10.1088/1748-9326/3/4/045022, 2008.

Lohmann, U., Rotstayn, L., Storelvmo, T., Jones, A., Menon, S., Quaas, J., Ekman, A. M. L., Koch, D., and Ruedy, R.: Total aerosol effect: radiative forcing or radiative flux perturbation?, Atmos. Chem. Phys., 10, 3235–3246, doi:10.5194/acp-10-3235-2010, 2010.

Mahowald, N. M., Muhs, D. R., Levis, S., Rasch, P. J., Yoshioka, M., Zender, C. S., and Luo, C.: Change in atmospheric mineral aerosols in response to climate: last glacial period, preindustrial, modern, and doubled carbon dioxide climates, J. Geophys. Res., 111, D10202, doi:10.1029/2005jd006653, 2006a.

Mahowald, N. M., Yoshioka, M., Collins, W. D., Conley, A. J., Fillmore, D. W., and Coleman, D. B.: Climate response and radiative forcing from mineral aerosols during the last glacial maximum, pre-industrial, current and doubled-carbon dioxide climates, Geophys. Res. Lett., 33, L20705, doi:10.1029/2006gl026126, 2006b.

Martensson, E. M., Nilsson, E. D., de Leeuw, G., Cohen, L. H., and Hansson, H. C.: Laboratory simulations and parameterization of the primary marine aerosol production, J. Geophys. Res., 108, 4297, doi:10.1029/2002jd002263, 2003.

Matsui, T., Masunaga, H., Kreidenweis, S. M., Pielke, R. A., Tao, W. K., Chin, M., and Kaufman, Y. J.: Satellite-based assessment of marine low cloud variability associated with aerosol, atmospheric stability, and the diurnal cycle, J. Geophys. Res., 111, D17204, doi:10.1029/2005jd006097, 2006.

McComiskey, A., Feingold, G., Frisch, A. S., Turner, D. D., Miller, M. A., Chiu, J. C.,





ACPD
11, 3399–3459, 2011



Min, Q. L., and Ogren, J. A.: An assessment of aerosol-cloud interactions in marine stratus clouds based on surface remote sensing, J. Geophys. Res., 114, D09203, doi:10.1029/2008jd011006, 2009.
Menon, S. and Rotstayn, L.: The radiative influence of aerosol effects on liquid-phase cumulus and stratiform clouds based on sensitivity studies with two climate models, Climate Dyn., 27, 345–356, doi:10.1007/S00382-006-0139-3, 2006.
Mlawer, E. J., Taubman, S. J., Brown, P. D., Iacono, M. J., and Clough, S. A.: Radiative transfer for inhomogeneous atmospheres: RRTM, a validated correlated-k model for the longwave, J. Geophys. Res., 102, 16663–16682, 1997.
Morrison, H. and Gettelman, A.: A new two-moment bulk stratiform cloud microphysics scheme in the community atmosphere model, version 3 (CAM3), Part I: Description and numerical tests, J. Climate, 21, 3642–3659, doi:10.1175/2008jcli2105.1, 2008.
Morrison, H. and Pinto, J. O.: Mesoscale modeling of springtime Arctic mixed-phase stratiform clouds using a new two-moment bulk microphysics scheme, J. Atmos. Sci., 62, 3683–3704, 2005.
Morrison, H., Curry, J. A., and Khvorostyanov, V. I.: A new double-moment microphysics parameterization for application in cloud and climate models, Part I: Description, J. Atmos. Sci., 62, 1665–1677, 2005.
Morrison, H., Thompson, G., and Tatarskii, V.: Impact of cloud microphysics on the development of trailing stratiform precipitation in a simulated squall line: comparison of one- and two-moment schemes, Mon. Weather Rev., 137, 991–1007, doi:10.1175/2008mwr2556.1, 2009.
Murphy, D. M., Solomon, S., Portmann, R. W., Rosenlof, K. H., Forster, P. M., and Wong, T.: An observationally based energy balance for the Earth since 1950, J. Geophys. Res., 114, D17107, doi:10.1029/2009jd012105, 2009.
Pincus, R. and Klein, S. A.: Unresolved spatial variability and microphysical process rates in large-scale models, J. Geophys. Res., 105, 27059–27065, 2000.
Platnick, S., Durkee, P. A., Nielsen, K., Taylor, J. P., Tsay, S. C., King, M. D., Ferek, R. J., Hobbs, P. V., and Rottman, J. W.: The role of background cloud microphysics in the radiative formation of ship tracks, J. Atmos. Sci., 57, 2607–2624, 2000.
Platnick, S., King, M. D., Ackerman, S. A., Menzel, W. P., Baum, B. A., Riedi, J. C., and Frey, R. A.: The MODIS cloud products: algorithms and examples from Terra, IEEE T. Geosci. Remote, 41, 459–473, 2003.
Quaas, J., Boucher, O., and Lohmann, U.: Constraining the total aerosol indirect effect in the





ACPD
11, 3399–3459, 2011



LMDZ and ECHAM4 GCMs using MODIS satellite data, Atmos. Chem. Phys., 6, 947–955, doi:10.5194/acp-6-947-2006, 2006.

Quaas, J., Ming, Y., Menon, S., Takemura, T., Wang, M., Penner, J. E., Gettelman, A., Lohmann, U., Bellouin, N., Boucher, O., Sayer, A. M., Thomas, G. E., McComiskey, A., Feingold, G., Hoose, C., Kristjánsson, J. E., Liu, X., Balkanski, Y., Donner, L. J., Ginoux, P. A., Stier, P., Grandey, B., Feichter, J., Sednev, I., Bauer, S. E., Koch, D., Grainger, R. G., Kirkevåg, A., Iversen, T., Seland, Ø., Easter, R., Ghan, S. J., Rasch, P. J., Morrison, H., Lamarque, J.-F., Iacono, M. J., Kinne, S., and Schulz, M.: Aerosol indirect effects – general circulation model intercomparison and evaluation with satellite data, Atmos. Chem. Phys., 9, 8697–8717, doi:10.5194/acp-9-8697-2009, 2009.

Quaas, J., Stevens, B., Stier, P., and Lohmann, U.: Interpreting the cloud cover – aerosol optical depth relationship found in satellite data using a general circulation model, Atmos. Chem. Phys., 10, 6129–6135, doi:10.5194/acp-10-6129-2010, 2010.

Randall, D., Khairoutdinov, M., Arakawa, A., and Grabowski, W.: Breaking the cloud parameterization deadlock, B. Am. Meteorol. Soc., 84, 1547, doi:10.1175/Bams-84-11-1547, 2003.

Rossow, W. B. and Schiffer, R. A.: Advances in understanding clouds from ISCCP, B. Am. Meteorol. Soc., 80, 2261–2287, 1999.

Rotstayn, L. D.: On the "tuning" of autoconversion parameterizations in climate models, J. Geophys. Res., 105, 15495–15507, 2000.

Small, J. D., Chuang, P. Y., Feingold, G., and Jiang, H. L.: Can aerosol decrease cloud lifetime?, Geophys. Res. Lett., 36, L16806, doi:10.1029/2009gl038888, 2009.

Stevens, B. and Feingold, G.: Untangling aerosol effects on clouds and precipitation in a buffered system, Nature, 461, 607–613, doi:10.1038/Nature08281, 2009.

Suzuki, K., Nakajima, T., Numaguti, A., Takemura, T., Kawamoto, K., and Higurashi, A.: A study of the aerosol effect on a cloud field with simultaneous use of GCM modeling and satellite observation, J. Atmos. Sci., 61, 179–194, 2004.

Suzuki, K., Nakajima, T., Satoh, M., Tomita, H., Takemura, T., Nakajima, T. Y., and Stephens, G. L.: Global cloud-system-resolving simulation of aerosol effect on warm clouds, Geophys. Res. Lett., 35, L19817, doi:10.1029/2008gl035449, 2008.

Tao, W. K., Chern, J. D., Atlas, R., Randall, D., Khairoutdinov, M., Li, J. L., Waliser, D. E., Hou, A., Lin, X., Peters-Lidard, C., Lau, W., Jiang, J., and Simpson, J.: A multiscale modeling system developments, applications, and critical issues, B. Am. Meteorol. Soc., 90, 515, doi:10.1175/2008bams2542.1, 2009.





ACPD
11, 3399–3459, 2011



Thompson, G., Rasmussen, R. M., and Manning, K.: Explicit forecasts of winter precipitation using an improved bulk microphysics scheme, Part I: description and sensitivity analysis, Mon. Weather Rev., 132, 519–542, 2004.
Waliser, D. E., Li, J. L. F., Woods, C. P., Austin, R. T., Bacmeister, J., Chern, J., Del Genio, A., Jiang, J. H., Kuang, Z. M., Meng, H., Minnis, P., Platnick, S., Rossow, W. B., Stephens, G. L., Sun-Mack, S., Tao, W. K., Tompkins, A. M., Vane, D. G., Walker, C., and Wu, D.: Cloud ice: a climate model challenge with signs and expectations of progress, J. Geophys. Res., 114, D00A21, doi:10.1029/2008JD010015, 2009.
Wang, M. and Penner, J. E.: Aerosol indirect forcing in a global model with particle nucleation, Atmos. Chem. Phys., 9, 239–260, doi:10.5194/acp-9-239-2009, 2009.
Wang, M. and Penner, J. E.: Cirrus clouds in a global climate model with a statistical cirrus cloud scheme, Atmos. Chem. Phys., 10, 5449–5474, doi:10.5194/acp-10-5449-2010, 2010.
Wang, M., Ghan, S., Easter, R., Ovchinnikov, M., Liu, X., Kassianov, E., Qian, Y., Gustafson, W., Larson, V. E., Schanen, D. P., Khairoutdinov, M., and Morrison, H.: The multi-scale aerosol-climate model PNNL-MMF: model description and evaluation, Geosci. Model Dev. Discuss., 3, 1625–1695, doi:10.5194/gmdd-3-1625-2010, 2010.
Wang, M. H., Penner, J. E., and Liu, X. H.: Coupled IMPACT aerosol and NCAR CAM3 model: evaluation of predicted aerosol number and size distribution, J. Geophys. Res., 114, D06302, doi:10.1029/2008jd010459, 2009.
Weng, F. Z. and Grody, N. C.: Retrieval of cloud liquid water using the Special Sensor Microwave Imager (SSM/I), J. Geophys. Res., 99, 25535–25551, 1994.
Wolff, E. W. and Cachier, H.: Concentrations and seasonal cycle of black carbon in aerosol at a coastal Antarctic station, J. Geophys. Res., 103, 11033–11041, 1998.
Wylie, D., Jackson, D. L., Menzel, W. P., and Bates, J. J.: Trends in global cloud cover in two decades of HIRS observations, J. Climate, 18, 3021–3031, 2005.
Xue, H. W., Feingold, G., and Stevens, B.: Aerosol effects on clouds, precipitation, and the organization of shallow cumulus convection, J. Atmos. Sci., 65, 392–406, doi:10.1175/2007jas2428.1, 2008.
Yoshioka, M., Mahowald, N. M., Conley, A. J., Collins, W. D., Fillmore, D. W., Zender, C. S., and Coleman, D. B.: Impact of desert dust radiative forcing on Sahel precipitation: relative importance of dust compared to sea surface temperature variations, vegetation changes, and greenhouse gas warming, J. Climate, 20, 1445–1467, doi:10.1175/Jcli4056.1, 2007.
Zender, C. S., Bian, H. S., and Newman, D.: Mineral dust entrainment and deposition





ACPD
11, 3399–3459, 2011



(DEAD) model: description and 1990s dust climatology, J. Geophys. Res., 108, 4416, doi:10.1029/2002jd002775, 2003.

Zhang, J. H., Lohmann, U., and Stier, P.: A microphysical parameterization for convective clouds in the ECHAM5 climate model: single-column model results evaluated at the Oklahoma atmospheric radiation measurement program site, J. Geophys. Res., 110, D15S07, doi:10.1029/2004jd005128, 2005.





ACPD

11, 3399–3459, 2011



**Table 1.** Annual global mean cloud and radiation parameters from MMF and CAM5 simulations (PD and PI) and observations: total cloud fraction (CLDTOT), low cloud fraction (CDLLOW), high cloud fraction (CLDHGH), shortwave cloud forcing (SWCF), longwave cloud forcing (LWCF), column-integrated grid-mean hydrometeor water path (LWP, liquid water path; RWP, rain water path; IWP, ice water path; SWP, snow water path; GWP, graupel water path; TIWP, total ice water path, and TIWP = IWP + SWP + GWP), column-integrated grid-mean hydrometeor number concentrations ($N_d$, cloud droplets; $N_i$, ice crystals; $N_r$, rain droplets; $N_s$, snow crystals; $N_g$, graupel particles), cloud-top droplet number concentrations ($N_{dtop}$) and droplet effective radius ($Reff_{top}$) for low level warm clouds, precipitation rate (Precip), column-integrated water vapor (Wmv), AOD, whole-sky shortwave (FSNT) and longwave (FLNT) radiative fluxes at the top of the atmosphere, clear-sky shortwave (FSNTC) and longwave (FLNTC) radiative fluxes at the top of the atmosphere.

| | MMF (PD) | MMF (PI) | CAM5 (PD) | CAM5 (PI) | Obs |
|---|---|---|---|---|---|
| CLDTOT (–) | 55.79% | 55.75% | 62.66% | 62.49% | 65–75[a] |
| CLDLOW (–) | 36.66% | 36.63% | 41.47% | 41.11% | # |
| CLDHGH (–) | 29.17% | 29.20% | 37.61% | 37.4% | 21–33[b] |
| SWCF ($W\,m^{-2}$) | −50.49 | −49.72 | −50.12 | −48.33 | −47 to −54[c] |
| LWCF ($W\,m^{-2}$) | 25.96 | 26.02 | 21.88 | 21.51 | 29–30[c] |
| LWP ($g\,m^{-2}$) | 55.88 | 53.77 | 48.38 (29.95)[d] | 44.45 (25.91)[d] | 50–87[e] |
| RWP ($g\,m^{-2}$) | 30.90 | 32.48 | 16.14 | 16.18 | # |
| IWP ($g\,m^{-2}$) | 9.91 | 9.91 | 16.08 (7.84)[d] | 16.14 (7.72)[d] | # |
| SWP ($g\,m^{-2}$) | 53.44 | 53.65 | 45.20 | 45.20 | # |
| GWP ($g\,m^{-2}$) | 5.69 | 5.47 | # | # | # |
| TIWP ($g\,m^{-2}$) | 69.04 | 69.03 | 61.28 | 61.34 | 10–80[f] |
| $N_d$ ($10^{10}\,m^{-2}$) | 2.28 | 1.80 | 1.53 | 1.09 | # |
| $N_i$ ($10^{10}\,m^{-2}$) | 0.0212 | 0.0214 | 0.010 | 0.0096 | # |
| $N_r$ ($10^{10}\,m^{-2}$) | 1.05e-3 | 1.29e-3 | 9.96e-4 | 1.08e-3 | # |
| $N_s$ ($10^{10}\,m^{-2}$) | 1.30e-3 | 1.30e-3 | 1.64e-3 | 1.62e-3 | # |
| $N_g$ ($10^{10}\,m^{-2}$) | 6.35e-6 | 6.37e-6 | # | # | # |
| $N_{dtop}$ ($cm^{-3}$) | 109.33 | 84.97 | 120.64 | 91.00 | # |





ACPD
11, 3399–3459, 2011



**Table 1.** Continued.

| | MMF (PD) | MMF (PI) | CAM5 (PD) | CAM5 (PI) | Obs |
|---|---|---|---|---|---|
| $Reff_{top}$ (μm) | 9.17 | 9.69 | 8.96 | 9.41 | 11.4–15.7[g] |
| Precip(mm $day^{-1}$) | 2.85 | 2.86 | 2.95 | 2.97 | 2.61[h] |
| Wmv (kg $m^{-2}$) | 25.47 | 25.46 | 25.87 | 25.75 | 24.6[i] |
| AOD (–) | 0.139 | 0.115 | 0.136 | 0.117 | 0.15[j] |
| FSNT (W $m^{-2}$) | 235.36 | 236.67 | 237.28 | 239.53 | 234–240[c] |
| FLNT (W $m^{-2}$) | 232.91 | 233.17 | 235.10 | 235.69 | 234–240[c] |
| FSNTC (W $m^{-2}$) | 285.88 | 286.42 | 287.42 | 287.87 | 287–289[c] |
| FLNTC (W $m^{-2}$) | 258.87 | 259.18 | 256.98 | 257.20 | 264–269[c] |

[a] Total cloud fraction observations are obtained from ISCCP for the years 1983–2001 (Rossow and Schiffer, 1999), MODIS data for the years 2001–2004 (Platnick, 2003) and HIRS data for the years 1979–2001 (Wylie et al., 2005).

[b] High cloud fraction observations are obtained from ISCCP data for the years 1983–2001 and HIRS for the years 1979–2001.

[c] SWCF, LWCF, FSNT, FSNTC, FLNT, and FLNTC are taken from ERBE for the years 1985–1989 (Kiehl and Trenberth, 1997) and CERES for the years 2000–2005 (http://science.larc.nasa.gov/ceres).

[d] Numbers in parenthesis are from large-scale clouds.

[e] Liquid water path is derived from SSM/I (for the years 1987–1994, Ferraro et al., 1996; for August 1993 and January 1994, Weng and Grody, 1994; and for August 1987 and February 1988, Greenwald et al., 1993) and ISCCP for the year 1987 (Han et al., 1994). SSM/I data are restricted to oceans.

[f] Total ice water path is from NOAA NESDIS, ISCCP, MODIS, and CloudSat (Fig. 18 in Waliser et al., 2009).

[g] Cloud-top droplet effective radius is obtained from ISCCP for the year 1987 (Han et al., 1994) and from MODIS (version 4) for the year 2001 (Platnick et al., 2003).

[h] Precipitation rate is taken from the Global Precipitation Climatology Project (GPCP) for the years 1979–2003 (http://www.gewex.org/gpcpdata).

[i] Precipitable water is from the NASA Water Vapor Project (NVAP) for the years 1988–1999 (http://eosweb.larc.nasa.gov/PRODOCS/nvap/table_nvap.html).

[j] AOD is from a satellite retrieval composite (Kinne et al., 2006).





ACPD
11, 3399–3459, 2011



**Table 2.** Global annual budgets of sulfate, BC, POM, SOA, dust and sea salt in the PD and PI simulations of the MMF and CAM5. CAM5 results are in parenthesis. Dust and sea salt budgets are separated into fine mode (Aitken + accumulation) and coarse mode components. Units are days for lifetime, Tg for burdens and Tg $yr^{-1}$ for sources, except for sulfate where units are Tg S and Tg S $yr^{-1}$ for burdens and sources.

| | Sulfate | BC | POM | SOA | Fine Dust | Coarse Dust | Fine Sea Salt | Coarse Sea Salt |
|---|---|---|---|---|---|---|---|---|
| PD source | 59.75 (42.47) | 7.76 (7.76) | 50.28 (50.28) | 103.44 (103.44) | 75.87 (96.44) | 2295.20 (2917.22) | 122.82 (157.17) | 3564.24 (4627.10) |
| PD burden | 1.05 (0.53) | 0.14 (0.11) | 1.04 (0.77) | 1.83 (1.40) | 2.00 (2.00) | 19.40 (21.64) | 0.88 (0.95) | 11.29 (10.77) |
| PD lifetime | 6.41 (4.55) | 6.59 (5.14) | 7.55 (5.59) | 6.46 (4.94) | 9.62 (7.57) | 3.09 (2.71) | 2.62 (2.21) | 1.17 (0.85) |
| PI source | 25.82 (15.24) | 3.08 (3.08) | 31.64 (31.64) | 92.68 (92.68) | 83.84 (101.07) | 2536.11 (3057.35) | 124.73 (156.49) | 3590.88 (4605.44) |
| PI burden | 0.45 (0.17) | 0.06 (0.04) | 0.67 (0.46) | 1.57 (1.21) | 2.16 (2.07) | 21.13 (22.63) | 0.86 (0.92) | 11.11 (10.63) |
| PI lifetime | 6.36 (4.07) | 7.11 (4.74) | 7.73 (5.31) | 6.18 (4.77) | 9.40 (7.48) | 3.04 (2.70) | 2.52 (2.15) | 1.13 (0.84) |
| PD/PI lifetime | 1.01 (1.12) | 0.93 (1.09) | 0.98 (1.05) | 1.04 (1.04) | 1.02 (1.01) | 1.01 (1.00) | 1.04 (1.03) | 1.02 (1.01) |





ACPD
11, 3399–3459, 2011



**Table 3.** Changes in global annual mean cloud and radiative parameters between the PI and PD simulations (PD–PI) in both the MMF and CAM5: aerosol optical depth (AOD), cloud-top droplet number concentrations ($N_{dtop}$), cloud-top droplet effective radius ($Reff_{top}$), liquid water path (LWP), shortwave (SWCF) and longwave (LWCF) cloud forcing, clear-sky (FSNTC) and whole-sky (FSNT) shortwave radiative fluxes at the top of the atmosphere, and whole-sky longwave radiative flux (FLNT) at the top of the atmosphere. For CAM5 LWP, the change in large-scale cloud LWP is in parenthesis.

| | AOD (–) | $N_{dtop}$ ($cm^{-3}$) | $Reff_{top}$ (μm) | LWP ($g\,m^{-2}$) | SWCF ($W\,m^{-2}$) | LWCF ($W\,m^{-2}$) | FSNTC ($W\,m^{-2}$) | FSNT ($W\,m^{-2}$) | FLNT ($W\,m^{-2}$) |
|---|---|---|---|---|---|---|---|---|---|
| MMF | 0.024 | 24.4 | −0.52 | 2.11 | −0.77 | −0.06 | −0.54 | −1.31 | 0.26 |
| CAM5 | 0.019 | 29.6 | −0.45 | 3.93 (4.04) | −1.79 | 0.37 | −0.45 | −2.25 | 0.59 |





ACPD
11, 3399–3459, 2011



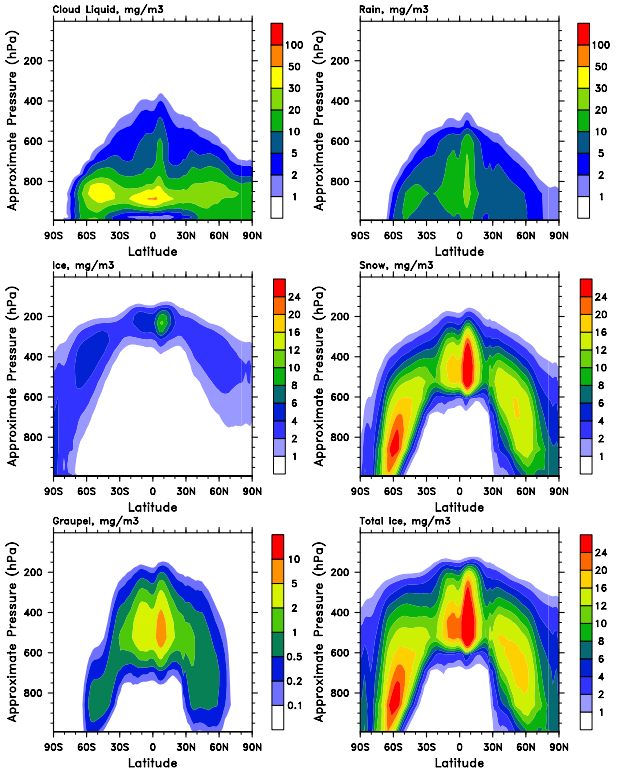


**Fig. 1.** Annual-averaged zonal-mean grid-mean mass concentrations ($\mathrm{mg\,m^{-3}}$) of cloud liquid water, rain water, ice water, snow water, graupel water, and total ice water (ice + snow + graupel) in PD in the MMF. The host GCM model (CAM5) uses a hybrid vertical coordinate and the pressure at the $k$th model level is given by $p(k) = A(k)p_0 + B(k)p_s$, where $p_s$ is surface pressure, $p_0$ is a specified constant pressure (1000 hPa), and $A$ and $B$ are coefficients. Data are plotted as a function of this hybrid vertical coordinate times 1000, and labelled "approximate pressure".





ACPD
11, 3399–3459, 2011



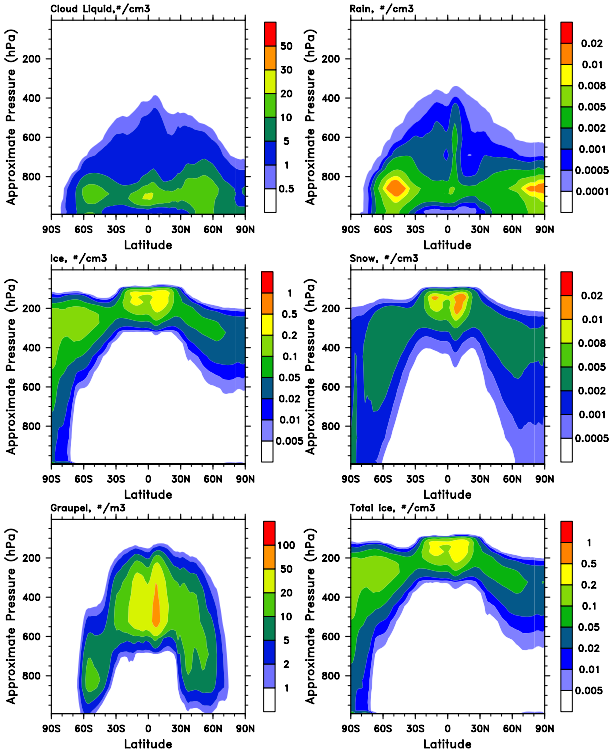


**Fig. 2.** The same as Fig. 1, but for hydrometeor number concentrations (units: $m^{-3}$ for grauple, and $cm^{-3}$ for other hydrometeors).





ACPD
11, 3399–3459, 2011



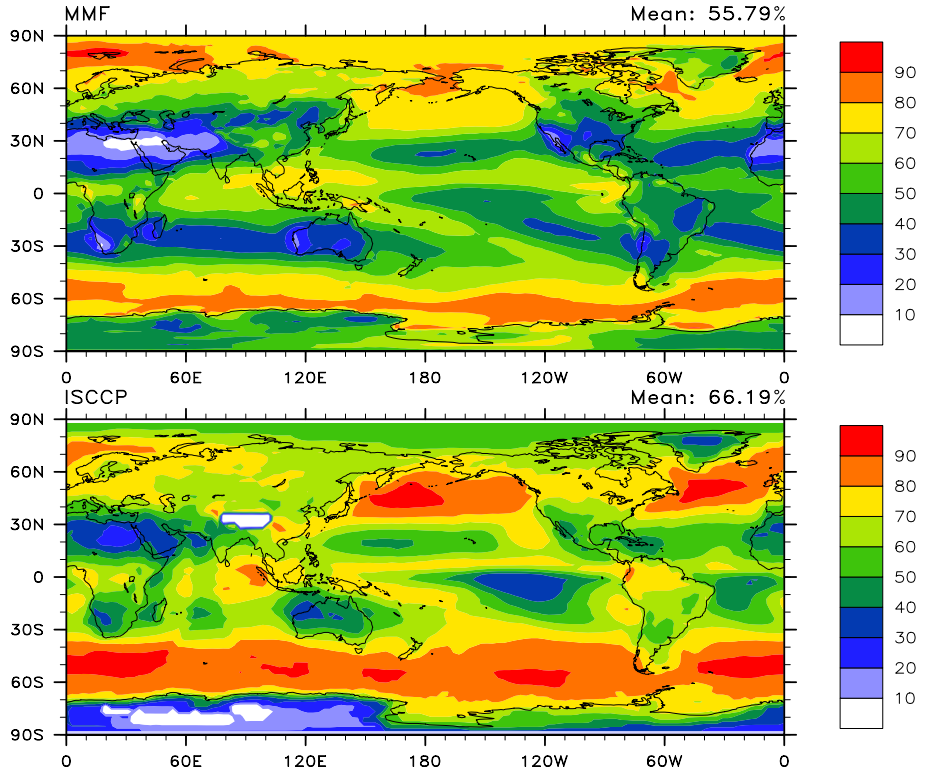


**Fig. 3.** PD annual average cloud fraction from the MMF model (upper panel) and from the ISCCP observations (lower panel).





ACPD
11, 3399–3459, 2011



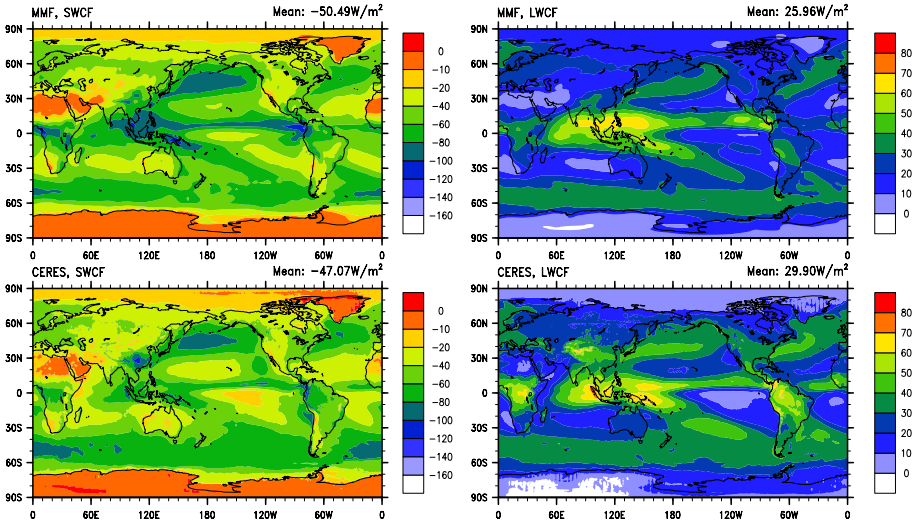


**Fig. 4.** PD annual average shortwave (left panels) and longwave (right panels) cloud forcing from the MMF model (upper panels) and from the CERES observations (lower panels).





ACPD
11, 3399–3459, 2011



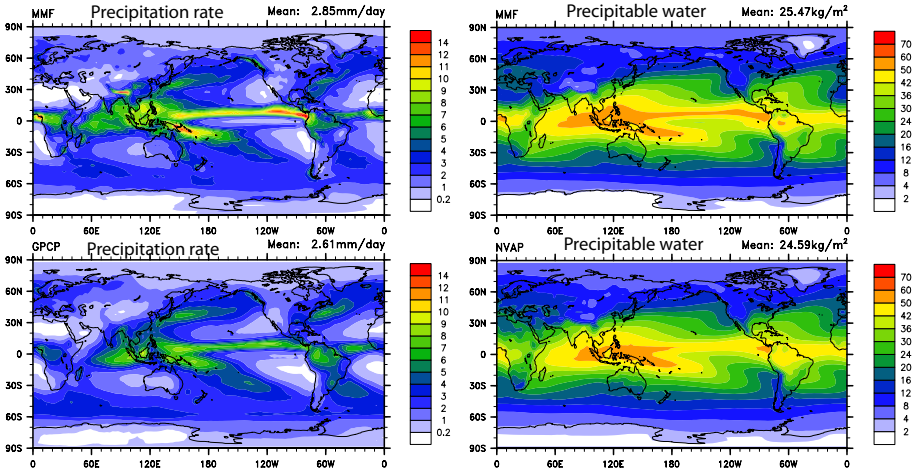


**Fig. 5.** PD annual average precipitation rate (left panels) and precipitable water (right panels) from the MMF model (upper panels) and from the observations (lower panels: precipitation rate from the GPCP observations and precipitable water from the NVAP observations).





ACPD
11, 3399–3459, 2011



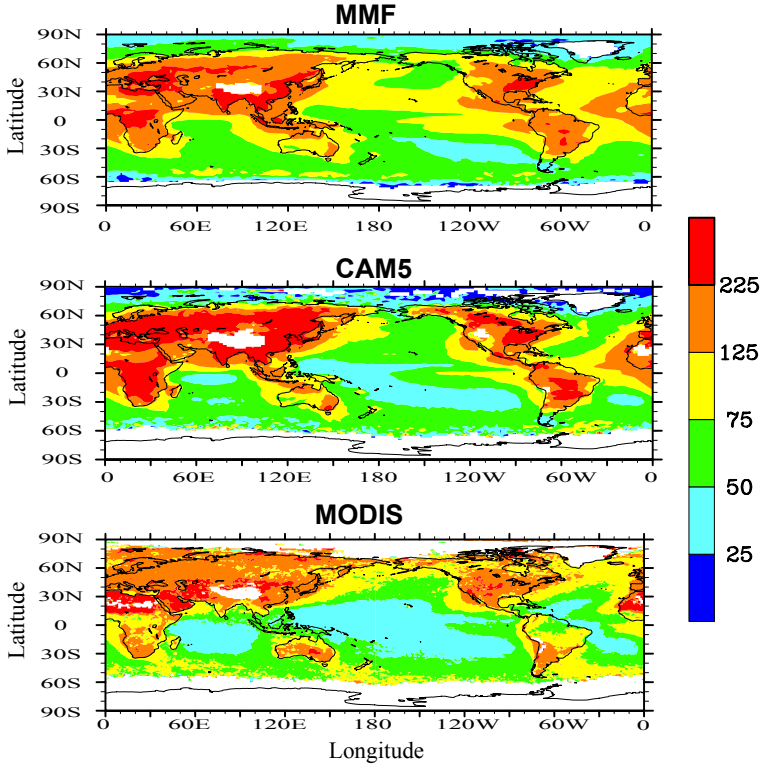


**Fig. 6.** PD annual-averaged cloud-top droplet number concentrations ($cm^{-3}$) derived from the MMF (upper panel), CAM5 (middle panel) and MODIS (lower panel).





ACPD
11, 3399–3459, 2011



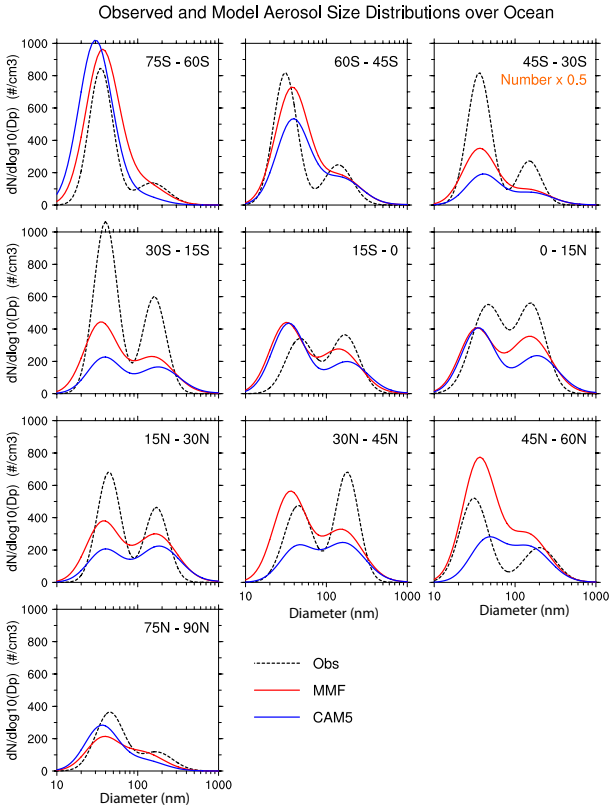


**Fig. 7.** PD aerosol size distributions in the marine boundary layer from the MMF, CAM5, and observations. Observations (Obs) are from Heintzenberg et al. (2000). For the 45° S–30° S latitude band, aerosol number density is scaled by 0.5 so the same *y* axis can be used for all latitude bands.





ACPD
11, 3399–3459, 2011



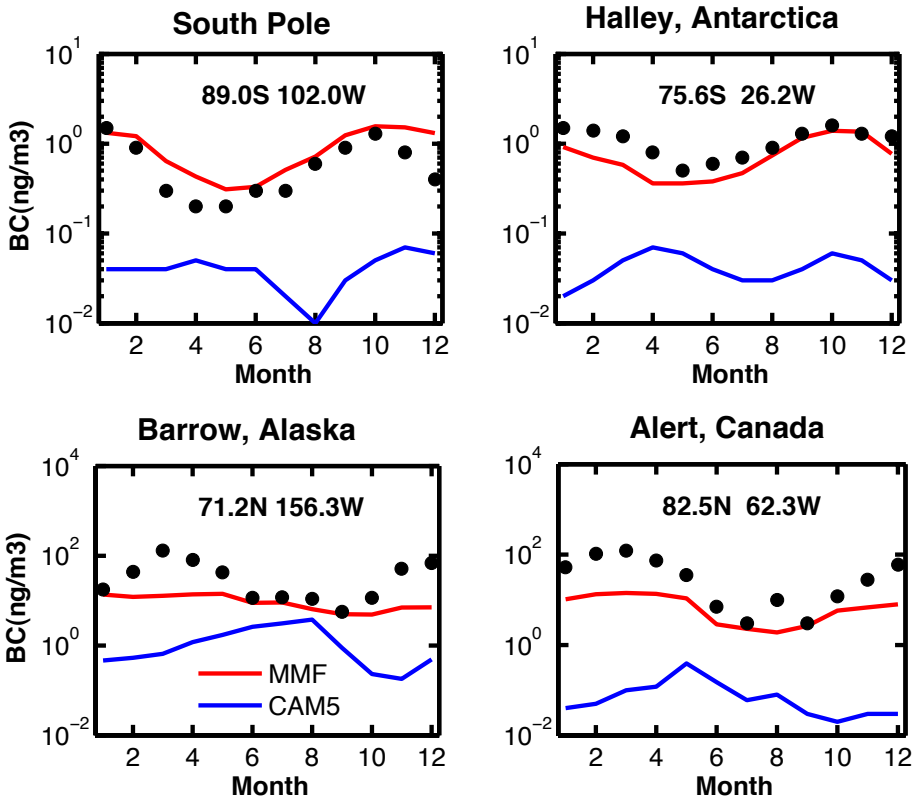


**Fig. 8.** Monthly-average BC concentrations at four polar sites: **(a)** Amndsen-Scott, South Pole (Bodhairne, 1995); **(b)** Halley, Antarctica (Wolff and Cachier, 1998); **(c)** Barrow, Alaska (Bodhaine, 1995); and **(d)** Alert, Canada (Hopper et al., 1994). PD model results are in solid lines (red: MMF; blue: CAM5), and observed data are in dots.





ACPD
11, 3399–3459, 2011



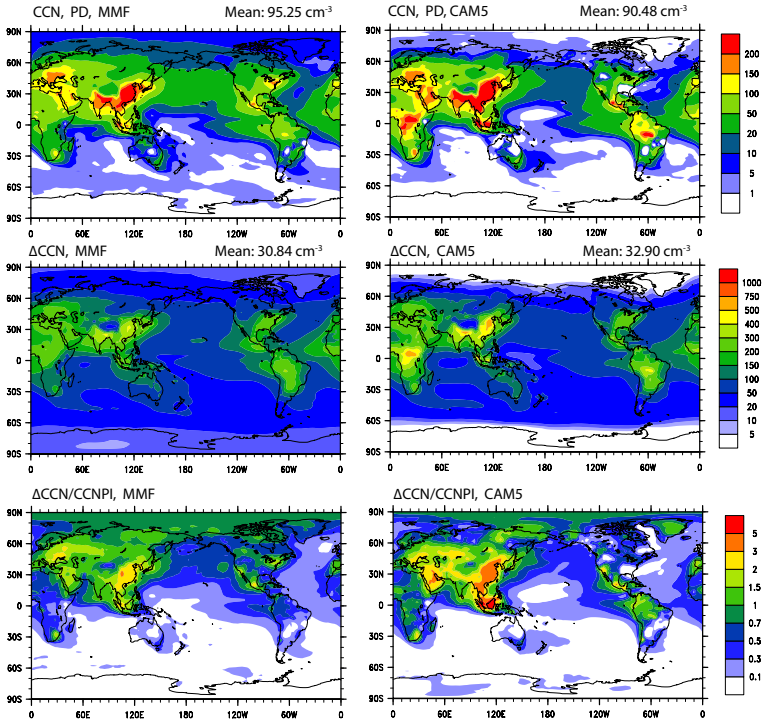


**Fig. 9.** Annual-averaged global distribution of CCN concentrations at 0.1% supersaturation averaged over the lowest 8 model levels (surface to about 800 hPa) in the PD simulations (top panels), the difference between PD and PI (PD–PI) (middle panels), and the relative differences between PD and PI (PD–PI/PI) (bottom panels) in both the MMF (left panels) and CAM5 (right panels).





ACPD
11, 3399–3459, 2011



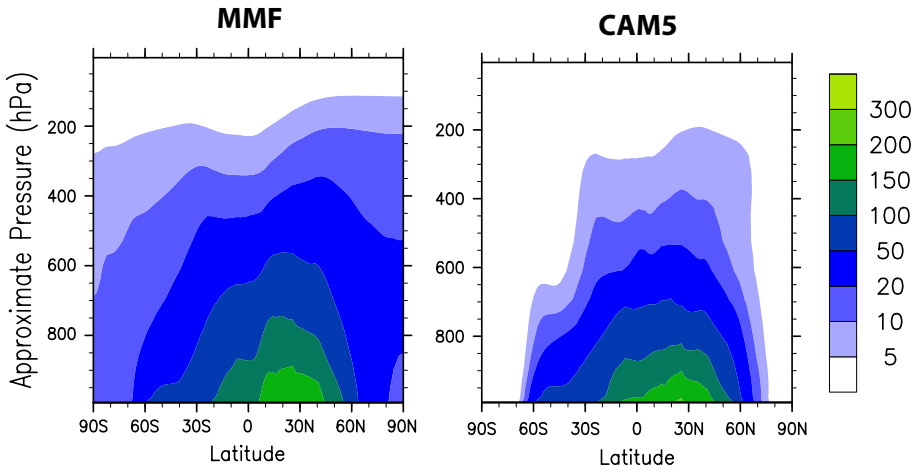


**Fig. 10.** Annual-averaged zonal-mean CCN concentrations at 0.1% supersaturation in the PD simulations in the MMF (left panel) and CAM5 (right panel).





ACPD
11, 3399–3459, 2011



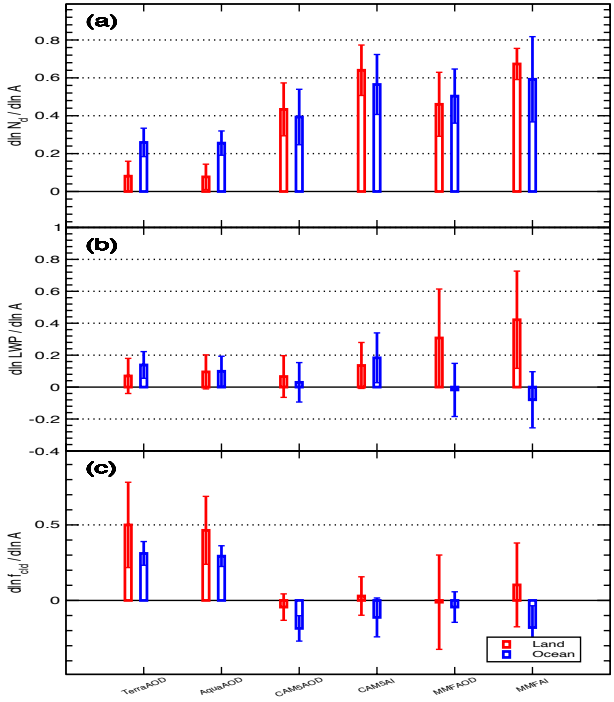


**Fig. 11.** Sensitivities of **(a)** cloud-top droplet number concentration, **(b)** cloud liquid water path, **(c)** cloud fraction to perturbations in column-integrated aerosol number concentration proxies represented by either AOD or AI as obtained from the linear regressions in PD. The weighted average for four seasons and all six land regions (red) and eight ocean regions (blue) is show, with the variability as error bar. Results are shown for MODIS Terra (TerraAOD: cloud parameters vs. AOD); MODIS Aqua (AquaAOD: cloud parameters vs. AOD); CAM5 (CAM5AOD: cloud parameters vs. AOD, CAM5AI: cloud parameters vs. AI); MMF (MMFAOD: cloud parameters vs. AOD, MMFAI: cloud parameters vs. AI).





ACPD
11, 3399–3459, 2011



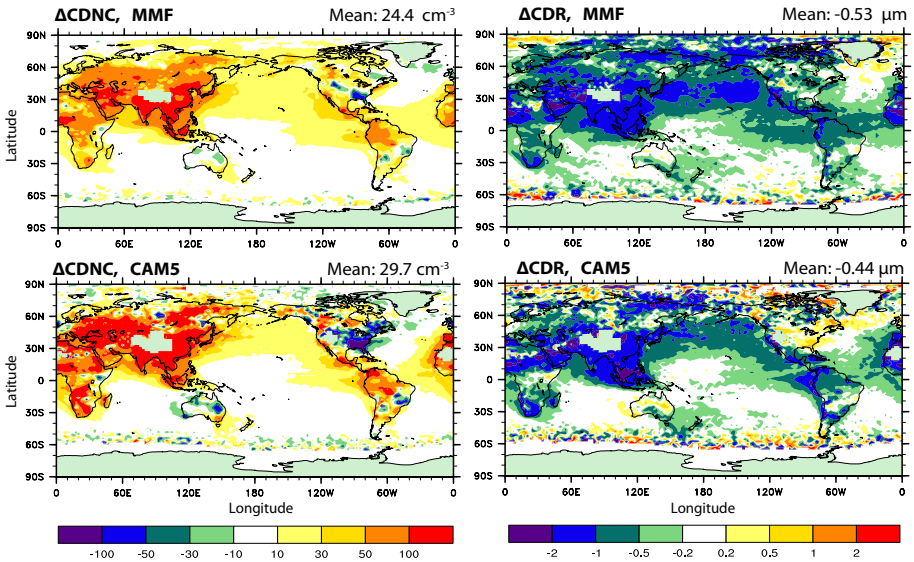


**Fig. 12.** Annual-average changes (PD–PI) in cloud-top droplet number concentrations (left panels) and cloud-top droplet effective radius (right panels) between the PD and PI simulations for low level (pressure > 640 hPa), warm clouds (cloud top temperature warmer than 273.16 K) in the MMF (upper panel) and CAM5 (lower panel).





ACPD
11, 3399–3459, 2011



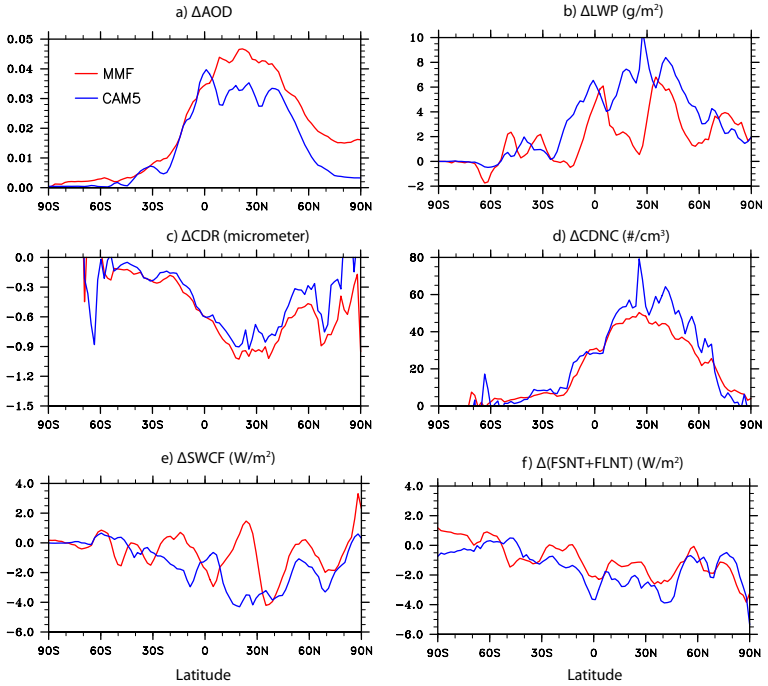


**Fig. 13.** Change in the zonal-mean annual-average AOD, liquid water path (LWP), cloud top droplet effective radius (CDR), cloud top droplet number concentrations (CDNC); shortwave cloud forcing (SWCF); and shortwave net flux at the top of the atmosphere (FSNT) from anthropogenic aerosols in both the MMF (red lines) and CAM5 (blue lines) simulations.





ACPD
11, 3399–3459, 2011



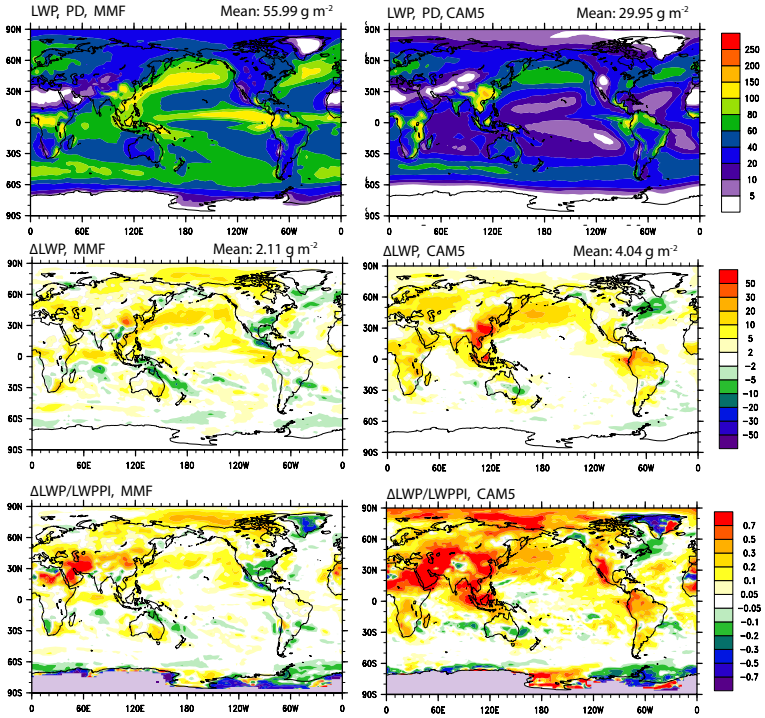


**Fig. 14.** Annual-averaged global distribution of liquid water path (LWP) in the PD simulations (top panels), the difference between PD and PI (PD–PI) (middle panels), and the relative differences between PD and PI (PD–PI/PI) (bottom panels) in both the MMF (left panels) and CAM5 (right panels). Liquid water path in CAM5 is from large-scale clouds only and does not include contributions from convective clouds.





ACPD
11, 3399–3459, 2011



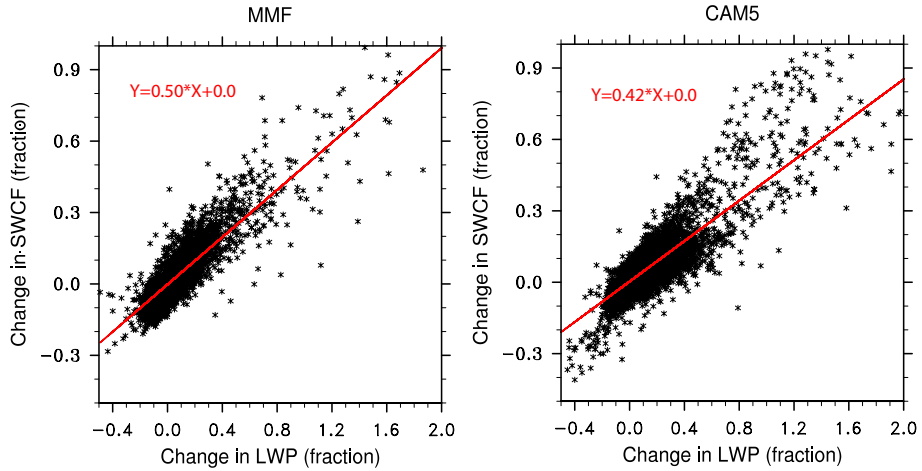


**Fig. 15.** Scatter plots and regressions of the relative changes [(PD–PI)/PI] in annual-mean shortwave cloud forcing (SWCF) versus the relative changes in annual-mean liquid water path (LWP) in both the MMF (left panel) and CAM5 (right panel) from PI to PD. Annual mean model data are sampled on each GCM grid column from 60° S to 60° N. LWP in CAM5 includes contributions from both large-scale and convective clouds. Red lines and equations are from the linear regression.





ACPD
11, 3399–3459, 2011



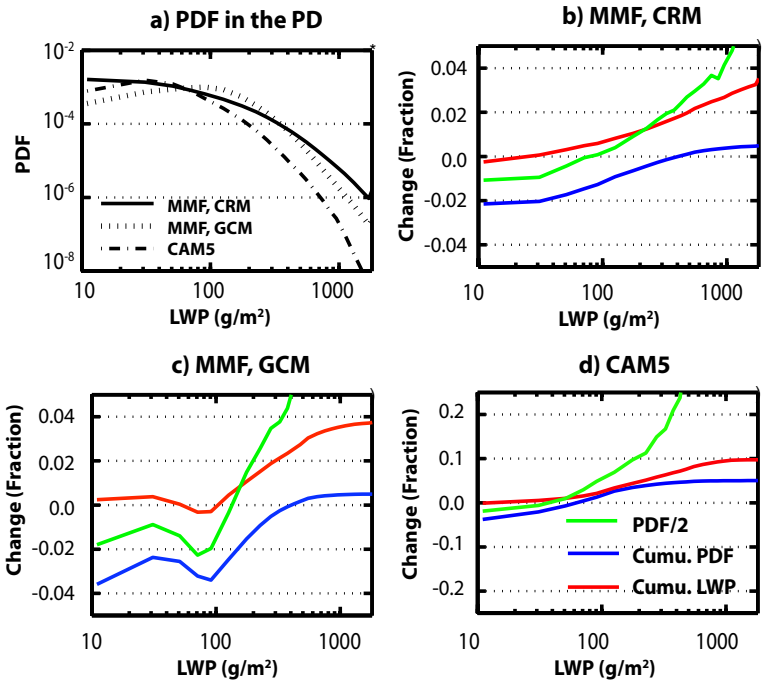


**Fig. 16. (a)** The PDFs of LWP in the PD simulations in the MMF and CAM5 (solid line is from the in-cloud LWP in CRM columns in the MMF; dotted line is from the in-cloud LWP in GCM columns in the MMF; and dash-dot line is from in-cloud LWP in GCM columns in CAM5); **(b–d)** relative changes in the PDF of (LWP) from PI to PD [(PD–PI)/PI] in both MMF and CAM5. The PDF of LWP are calculated from **(b)** the in-cloud LWP in CRM columns in MMF, **(c)** in-cloud LWP in GCM columns in MMF, and **(d)** in-cloud LWP in GCM columns in CAM5. Green lines are for the relative changes in the PDF of LWP (scaled by a factor of 0.5); blue lines are for the relative changes in the cumulative PDF of LWP; and red lines are for the relative changes in the cumulative LWP (for a given LWP bin, the cumulative LWP is the in-cloud LWP averaged from the smallest LWP bin to the given LWP bin).





ACPD
11, 3399–3459, 2011



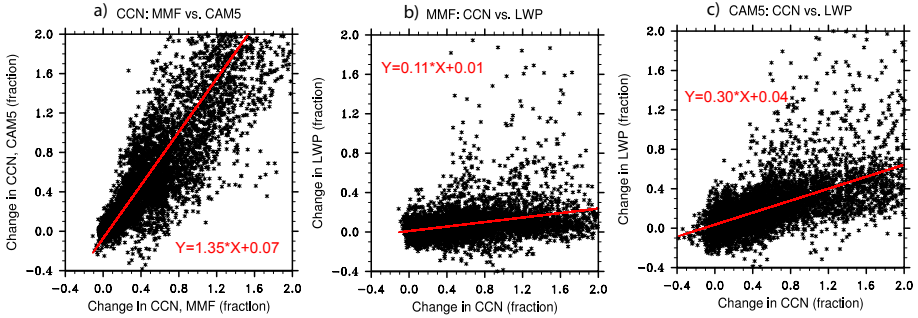


**Fig. 17.** Scatter plots and regressions of **(a)** the relative changes [(PD–PI)/PI] in annual-mean CCN concentrations (at 0.1% supersaturation) in CAM5 versus the MMF, **(b)** the relative changes in annual-mean liquid water path (LWP) versus the relative changes in annual-mean CCN concentrations in the MMF model, and **(c)** like **(b)** but in the CAM5 model. LWP in CAM5 only includes the contribution from large-scale clouds. Annual mean data are sampled on each GCM grid column from 60° S to 60° N. CCN concentrations are averaged over the lowest 8 model levels (surface to about 800 hPa). Red lines and equations are from the linear regression.





ACPD
11, 3399–3459, 2011